HHS Public Access

Author manuscript

Nat Metab. Author manuscript; available in PMC 2024 March 19.

Published in final edited form as:

Nat Metab. 2024 February ; 6(2): 304–322. doi:10.1038/s42255-024-00983-3.

Transcriptional programming of translation by BCL6 controls skeletal muscle proteostasis

Krithika Ramachandran[1], **Christopher R. Futtner**[1,2], **Meredith A. Sommars**[1], **Mattia Quattrocelli**[3,4,5], **Yasuhiro Omura**[1,2], **Ellen Fruzyna**[1], **Janice C. Wang**[1], **Nathan J. Waldeck**[1], **Madhavi D. Senagolage**[1], **Carmen G. Telles**[1], **Alexis R. Demonbreun**[3], **Erin Prendergast**[6], **Nicola Lai**[7], **Daniel Arango**[8], **Ilya R. Bederman**[6], **Elizabeth M. McNally**[3], **Grant D. Barish**[1,2,✉]

[1]Division of Endocrinology, Metabolism, and Molecular Medicine, Department of Medicine, Feinberg School of Medicine, Northwestern University, Chicago, IL, USA.

[2]Jesse Brown VA Medical Center, Chicago, IL, USA.

[3]Center for Genetic Medicine, Feinberg School of Medicine, Northwestern University, Chicago, IL, USA.

[4]Division of Molecular Cardiovascular Biology, Heart Institute, Cincinnati Children's Hospital Medical Center, Cincinnati, OH, USA.

[5]Department of Pediatrics, University of Cincinnati College of Medicine, Cincinnati, OH, USA.

[6]Department of Genetics and Genome Sciences, Case Western Reserve University, Cleveland, OH, USA.

[7]Department of Mechanical, Chemical, and Materials Engineering, University of Cagliari, Cagliari, Italy.

[8]Department of Pharmacology, Feinberg School of Medicine, Northwestern University, Chicago, IL, USA.

✉**Correspondence and requests for materials** should be addressed to Grant D. Barish. grant.barish@northwestern.edu.

Author contributions

Experiments were designed by G.D.B., K.R., C.R.F., A.R.D., I.R.B. and E.M.M. Experiments were performed by K.R., C.R.F., M.A.S., M.Q., Y.O., E.F., J.C.W., M.D.S., C.G.T., E.P. and I.R.B. Data analysis was done by K.R., C.R.F., M.A.S., E.F., G.D.B., N.L., I.R.B., D.A., N.J.W. and M.Q. The paper was written by K.R., C.R.F., D.A. and G.D.B. with input from the other authors.

Competing interests

The authors declare no competing interests.

Additional information

Extended data is available for this paper at https://doi.org/10.1038/s42255-024-00983-3.

Supplementary information The online version contains supplementary material available at https://doi.org/10.1038/s42255-024-00983-3.

Peer review information *Nature Metabolism* thanks Stuart Phillips, Marco Sandri and the other, anonymous, reviewer(s) for their contribution to the peer review of this work. Primary Handling Editor: Yanina-Yasmin Pesch, in collaboration with the *Nature Metabolism* team.

Reporting summary

Further information on research design is available in the Nature Portfolio Reporting Summary linked to this article.

Code availability

No custom code was used.

Abstract

Skeletal muscle is dynamically controlled by the balance of protein synthesis and degradation. Here we discover an unexpected function for the transcriptional repressor B cell lymphoma 6 (BCL6) in muscle proteostasis and strength in mice. Skeletal muscle-specific *Bcl6* ablation in utero or in adult mice results in over 30% decreased muscle mass and force production due to reduced protein synthesis and increased autophagy, while it promotes a shift to a slower myosin heavy chain fibre profile. Ribosome profiling reveals reduced overall translation efficiency in *Bcl6*-ablated muscles. Mechanistically, tandem chromatin immunoprecipitation, transcriptomic and translational analyses identify direct BCL6 repression of eukaryotic translation initiation factor 4E-binding protein 1 (*Eif4ebp1*) and activation of insulin-like growth factor 1 (*Igf1*) and androgen receptor (*Ar*). Together, these results uncover a bifunctional role for BCL6 in the transcriptional and translational control of muscle proteostasis.

The acquisition and maintenance of skeletal muscle mass are critical for motor and metabolic functions, but the mechanisms controlling muscle proteostasis remain incompletely understood[1,2]. Insulin/insulin-like growth factor 1 (IGF-1) signalling has emerged as a central regulator, leading to activation of AKT and mechanistic target of rapamycin complex 1 (mTORC1), which suppresses autophagy by phosphorylating ULK1 and enhances protein synthesis by phosphorylating S6 kinase (S6K) and 4EBP[3]. In addition, activated AKT phosphorylates FOXO transcription factors and localizes them to the cytoplasm, inhibiting expression of atrogenic targets including the ubiquitin ligases atrogin-1 and MuRF-1 (refs. 4,5). FOXO transcription factors act in conjunction with additional signalling cascades to mediate transcriptional control of skeletal muscle homeostasis. In particular, myostatin, a member of the transforming growth factor beta superfamily expressed and secreted predominantly by skeletal muscle, is a potent negative regulator of muscle growth that activates SMAD2/SMAD3 and suppresses AKT–mTORC1 signalling[6]. Conversely, bone morphogenetic proteins induce muscle hypertrophy by activating SMAD1/SMAD5/SMAD8 and mTOR signalling[7]. Androgens also increase muscle mass by enhancing IGF-1–AKT–mTORC1 signalling while suppressing myostatin and ubiquitin ligase expression[8]. Despite progress elucidating these and other regulators, important gaps remain in our understanding of transcriptional programmes and the precise mechanisms by which they control muscle proteostasis.

BCL6 is a transcriptional repressor recognized for its critical role in germinal centres and diffuse large B cell lymphomas but of virtually unknown function in skeletal muscle[9–11]. It controls transcription through sequence-specific DNA binding by its C2H2 zinc finger domain and interactions with corepressors including SMRT, NCoR, BCoR, CtBP, MTA3/NuRD and class I and II histone deacetylases (HDACs). Although initial characterization of BCL6 nearly 30 years ago detected high levels in adult skeletal muscle, its role therein has remained elusive[10]. In myogenic cell lines, BCL6 was shown to be induced during differentiation[12], and expression of *BCL6* in human skeletal muscle was inversely correlated to maximal oxygen uptake (VO_2 max), suggesting a role for BCL6 in metabolic programming[13]. Furthermore, BCL6 cofactors including class IIa HDACs and NCoR have been implicated in myofibre metabolism and muscle mass[14,15]. Collectively, these

observations pointed to the possibility that BCL6 could be an important transcriptional regulator in skeletal muscle.

Here, using tissue-specific constitutive and inducible genetic deletion, we reveal a role for *Bcl6* in skeletal muscle protein homeostasis. Loss of *Bcl6* in myofibres during mouse embryonic development led to reduced muscle mass, and inducible deletion in adult mice resulted in muscle atrophy. In both settings, loss of *Bcl6* led to decreased muscle force production. Using stable isotopic incorporation and non-linear kinetic modelling together with integrated analysis of RNA sequencing (RNA-seq), chromatin immunoprecipitation with sequencing (ChIP–seq) and ribosome sequencing (Ribo-seq) in vivo, we found that BCL6 controls muscle mass by directly regulating key genes involved in translational control and proteostatic signalling. Accordingly, *Bcl6* ablation reduces skeletal muscle protein synthesis by inhibiting early phases of mRNA translation and increasing autophagy. Together, our data establish BCL6 as a potent transcriptional determinant of translation and degradation in skeletal muscle.

Results

BCL6 is highly expressed in differentiated skeletal muscle

To begin to understand the role of BCL6 in skeletal muscle, we interrogated its expression across tissues of the body. Both in male and female mice, *Bcl6* was highly expressed in skeletal muscles compared to other solid organs, particularly within mixed or predominantly glycolytic muscles such as extensor digitorum longus (EDL) and quadriceps (Fig. 1a). Similarly, in human tissues from the Genotype-Tissue Expression (GTEx) project, *BCL6* is expressed highest in muscle, with levels nearly equivalent to those in whole blood (Fig. 1b). In line with these in vivo observations, *Bcl6* mRNA and corresponding protein were upregulated 2.4-fold and 2.9-fold, respectively, in cultured myotubes compared to myoblasts (Extended Data Fig. 1a,b). Given its robust expression, we examined active regulatory regions along the *Bcl6* locus in skeletal muscle. Using ChIP–seq datasets for the active enhancer marker acetylated histone 3 lysine 27 (H3K27ac)[16], we identified a putative super-enhancer within the muscle *Bcl6* locus (Fig. 1c). Together, these observations established BCL6 as a highly enriched transcription factor with potentially important roles in skeletal muscle identity and disease[17].

Developmental role of BCL6 in establishing muscle mass

To address the function of *Bcl6*, we crossed mice harbouring a floxed allele for *Bcl6* (*Bcl6*$^{fl/fl}$)[18] with animals expressing Cre recombinase from the human alpha-skeletal actin (HSA) promoter (Fig. 1d) to constitutively delete *Bcl6* in mature striated muscle fibres (*Bcl6*^{MKO} mice) beginning 9 d post coitum[19]. Comparing *Bcl6*^{MKO} mice to controls at 8 weeks of age, *Bcl6* mRNA was reduced by over 85% in skeletal muscles including the quadriceps, gastrocnemius and soleus but unchanged in the heart (Fig. 1e). Similarly, levels of BCL6 protein were diminished by 84% in the skeletal muscles of *Bcl6*^{MKO} animals, but not changed in heart (Fig. 1f and Extended Data Fig. 1c). Remarkably, although these mice were born at expected Mendelian ratios, males exhibited nearly 16% lower body weights and 19% reduced lean mass compared to controls (Fig. 1g). These changes were grossly apparent

after necropsy of male *Bcl6*^{MKO} mice, in which we found a 36–44% weight reduction in quadriceps, gastrocnemius, tibialis anterior (TA) and EDL, but no difference in the soleus (Fig. 1h,i). Females exhibited a similar but more modest 8% reduction in body weight and 10% lower lean body mass with 28–35% reduced muscle weights (Extended Data Fig. 1d,e). Histologically, we found a reduction in myofibre cross-sectional area (CSA) with no dystrophic features in *Bcl6*-ablated muscle (Fig. 1j). Frequency distributions of muscle fibre CSA showed a leftward shift to smaller fibres in *Bcl6*^{MKO} muscles compared to controls with an overall 35% reduction in the CSA of TA muscle (Fig. 1k). Thus, developmental loss of skeletal muscle *Bcl6* reduced skeletal muscle mass, particularly in glycolytic muscle groups.

Rapid muscle loss following muscle *Bcl6* deletion in adults

To determine whether the reduced muscle mass of *Bcl6*^{MKO} mice reflected a developmental defect, we next sought to test the impact of *Bcl6* ablation in adult skeletal muscle. We generated an inducible muscle *Bcl6*-knockout model (*Bcl6*$^{i\text{-}MKO}$) by crossing *Bcl6* floxed mice to animals expressing a gene fusion of Cre flanked by two mutated murine oestrogen receptors (AEC mice) under the control of the HSA promoter (Fig. 2a)[20]. This system allowed us to delete *Bcl6* by treating mice with four consecutive daily doses of tamoxifen. Within 1 week of tamoxifen treatment, *Bcl6* mRNA was reduced by 80–95% in various skeletal muscles of *Bcl6*$^{i\text{-}MKO}$ animals compared to corn oil-treated Cre-expressing control mice (Cre^{+} oil) or 72–90% compared to tamoxifen-treated Cre-negative control mice (Cre^{-} tmx; Fig. 2b). Although tamoxifen itself moderately reduced muscle *Bcl6* mRNA compared to corn oil treatment, BCL6 protein levels were not significantly different between the control groups, whereas BCL6 was reduced by over 90% in quadriceps from tamoxifen-treated *Bcl6*$^{i\text{-}MKO}$ mice (Fig. 2c). Levels of *Bcl6* mRNA and corresponding protein were similar in the hearts of both controls and inducible muscle knockout mice (Fig. 2b,c). We tested the impact of deleting *Bcl6* from adult muscles by treating male *Bcl6*$^{i\text{-}MKO}$ mice at 12 weeks of age with tamoxifen. Body weights and lean masses of *Bcl6*$^{i\text{-}MKO}$ mice reduced significantly compared to both controls within 2 weeks (Fig. 2d). By 12 weeks after tamoxifen treatment, muscle *Bcl6*-ablated mice showed an overall 5–7% reduction in body weight, and an 11% reduction in lean body mass compared to both controls with no change in fat mass (Fig. 2d). Consistent with these changes in body composition, muscle masses for quadriceps, gastrocnemius, TA and EDL muscles were 16–29% reduced compared to muscles from either control group (Fig. 2e). We observed highly similar effects after inducible muscle *Bcl6* deletion in younger cohorts treated with tamoxifen at only 8 weeks of age. In these studies, *Bcl6*$^{i\text{-}MKO}$ male mice exhibited 4–7% reduced weight and 10% reduced lean mass compared to controls (Extended Data Fig. 2a), while females exhibited 4–8% reduced weight and 7–10% reduced lean mass within 12 weeks after *Bcl6* ablation (Extended Data Fig. 2b). Moreover, necropsy of quadriceps, gastrocnemius, TA and EDL muscles revealed 27–32% reductions in mass compared to muscles from either control group in males (Extended Data Fig. 2c), and 19–23% reductions compared to either control in females (Extended Data Fig. 2d), with no loss in soleus mass. Similarly to constitutive *Bcl6* muscle knockouts, myofibre mass was diminished in *Bcl6*$^{i\text{-}MKO}$ muscles compared to Cre^{-} tmx controls, as shown by an overall 33% reduction in CSA (Fig. 2f,g). Thus, these data reveal a critical role for BCL6 in the postnatal maintenance of muscle mass.

Muscle atrophy is associated with reduced BCL6

Given that genetic loss of muscle *Bcl6* in adult mice led to atrophy, we next explored whether changes in BCL6 levels could play a pathophysiological role in muscle wasting conditions. C57BL/6 mice were fasted for 48 h, leading to a 15% reduction in skeletal muscle mass (Extended Data Fig. 2e), and we detected 50–70% reduced *BCL6* transcript and protein in their atrophic muscles (Extended Data Fig. 2f,g). We also mined published data from mouse models of cancer-associated cachexia and found that muscle *Bcl6* was significantly diminished in metastatic colon cancer (63% reduced) and trended lower in breast cancer and non-small-cell lung adenocarcinoma (55% and 18% reduced, respectively; Extended Data Fig. 2h)[21–23]. Based on the suppression of muscle *Bcl6* in these cancer models, we exposed differentiated C2C12 myotubes to cell-free conditioned media from colon-26 carcinoma and likewise observed significant reductions in *BCL6* transcript and protein (Extended Data Fig. 2i). To determine signals that control muscle *Bcl6* expression, we treated differentiated C2C12 myotubes with cytokines associated with cancer cachexia and hormones elicited by fasting (Extended Data Fig. 2j). We found that cytokines, particularly interleukin (IL)-6, and to a lesser extent IL-1B and tumour necrosis factor, reduced *Bcl6* mRNA expression. The suppressive effect of IL-6 was blocked by inhibiting STAT3, the major transcriptional mediator for IL-6 signalling (Extended Data Fig. 2j). Similarly, growth hormone, which activates signal transducer and activator of transcription (STAT) proteins, reduced *Bcl6* expression, while glucocorticoids (dexamethasone) had no effect. Collectively, these findings suggested that *Bcl6* is regulated by circulating cytokines and growth factors and may be an important mediator of muscle loss in undernutrition or cancer-associated wasting.

Bcl6 controls a slow to fast shift in myofibres

Muscle atrophy differentially affects slow-twitch and fast-twitch myofibres and can be associated with changes in myofibre composition[24,25]. Thus, to address the impact of *Bcl6* ablation on muscle myofibres, we quantified slow-twitch type 1 fibres and fast-twitch oxidative (2a), intermediate (2x) and glycolytic (2b) fibres using immunofluorescence with antibodies recognizing their characteristic myosin heavy chains. In the quadriceps of $Bcl6^{MKO}$ mice, we observed a 4.4-fold increase in type 1 fibres and 1.4-fold increase in 2a fibres with commensurate decreases in type 2x and 2b fibres compared to $Bcl6^{fl/fl}$ controls (Fig. 3a). This shift was also apparent in other muscle groups of $Bcl6^{MKO}$ mice. In the predominantly oxidative soleus muscle from $Bcl6^{MKO}$ mice, we detected a twofold increase in type 1 fibres and a complete loss of type 2b fibres (Fig. 3b). Furthermore, in the highly glycolytic EDL, nearly 11% of myofibres were type 1 in $Bcl6^{MKO}$ mice, while no type 1 fibres were detected in controls (Fig. 3c). We further confirmed our fibre typing results by quantitative PCR (qPCR) analysis and detected increased expression of slow troponins and myosin heavy chains (*Tnni1*, *Tnnt1* and *Myh7*) and reciprocally reduced expression of fast isoforms (*Tnni2, Tnnt3* and *Myh4*) in $Bcl6^{MKO}$ muscles (Fig. 3d). We performed similar fibre-type analysis in adult inducible $Bcl6^{i\text{-}MKO}$ mice 6 weeks after tamoxifen treatment (Extended Data Fig. 3a). In contrast to deletion during muscle development, adult deletion of *Bcl6* in the quadriceps led to only a modest 1.5-fold increase in type 1 fibres but a more remarkable 2.3-fold increase in type 2a fibres with corresponding reductions in 2x fibres. Next, we assessed muscle mitochondrial content by quantifying mitochondrial DNA and

western blotting for the mitochondrial membrane protein VDAC but found no changes in levels in *Bcl6*-knockout muscles (Extended Data Fig. 3b,c). We also interrogated respiratory chain mitochondrial complex subunits I–V and found that in *Bcl6*^{MKO} mice, complex II was significantly increased by 1.5-fold, while complex III and V trended higher (Extended Data Fig. 3d). Finally, we quantified changes in myofibre CSA according to myofibre type in *Bcl6*^{MKO} and *Bcl6*$^{i\text{-}MKO}$ mice compared to their respective controls. We found that myofibre CSAs were reduced most strikingly among type 2b fibres in both our *Bcl6* muscle knockout models (Extended Data Fig. 3e,f), resembling the preferential type 2b myofibre atrophy associated with starvation or cancer cachexia. Together, these results indicated that loss of muscle *Bcl6* caused a shift towards myosin heavy chains typically associated with oxidative metabolism but did not significantly increase mitochondrial content and could not explain the reduced mass of knockout tissues.

Bcl6 regulates skeletal muscle force production

To further assess the functional implications of reduced muscle mass in skeletal muscle *Bcl6*-deleted mice, we tested their forelimb grip strength. Male and female *Bcl6*^{MKO} mice were 26% and 11% weaker, respectively, than their sex-specific controls (Fig. 4a and Extended Data Fig. 4a). Similarly, 12 weeks after tamoxifen treatment, *Bcl6*$^{i\text{-}MKO}$ mice exhibited reduced forelimb grip strength by 14–17% in males and 8–11% in females compared to their controls (Fig. 4b and Extended Data Fig. 4b). Normalization to lean mass abrogated these differences in both male and female *Bcl6*^{MKO} and *Bcl6*$^{i\text{-}MKO}$ mice (Fig. 4a,b and Extended Data Fig. 4a,b), indicating that reduced strength in these muscle *Bcl6*-ablated animals was a consequence of decreased muscle mass. We next evaluated isometric muscle mechanics of TA muscles in live anaesthetized mice. *Bcl6*^{MKO} muscles produced 40% or 47% diminished maximum tetanic force in males or females, respectively (Fig. 4c and Extended Data Fig. 4c). Similarly, TAs of male *Bcl6*$^{i\text{-}MKO}$ mice exhibited nearly 40% reduced tetanic force (Fig. 4d). We also calculated the specific force normalized to muscle CSA in male mice and found no difference between *Bcl6*^{MKO} or *Bcl6*$^{i\text{-}MKO}$ mice and their respective controls, indicating a proportional relationship between mass and strength in *Bcl6*-deleted muscle (Fig. 4c,d). Reductions in maximum force produced by *Bcl6*^{MKO} and *Bcl6*$^{i\text{-}MKO}$ muscle were stable for 25 consecutive contraction bouts as seen by their fatigue curves (Fig. 4e,f), but when normalized to initial force, their relative fatigue was unaltered compared to controls (Fig. 4e,f). In sum, these data demonstrated that loss of *Bcl6* in skeletal muscle leads to atrophy-associated loss of strength.

In light of the increased slow myofibre content in muscle *Bcl6*-deleted mice, we tested their endurance and activity. *Bcl6*^{MKO} and inducibly ablated *Bcl6*$^{i\text{-}MKO}$ mice 12 weeks after tamoxifen treatment along with their respective controls were run to exhaustion on a treadmill, but we observed no impact for loss of *Bcl6* on endurance performance (Extended Data Fig. 4d,e). Furthermore, we assessed total activity via infra-red beam breaking but detected no difference among *Bcl6*^{MKO} mice or *Bcl6*$^{i\text{-}MKO}$ mice 10 d after tamoxifen treatment compared to controls (Extended Data Fig. 4f,g). These experiments demonstrated that the increase in slow myofibres was not reflected functionally in *Bcl6* muscle knockout mice. Moreover, altered activity could not explain their shifted myofibre profiles or contribute to atrophy from skeletal muscle unloading.

BCL6 directly controls proteostatic regulators in muscle

To begin to understand the gene regulatory basis by which BCL6 influences skeletal muscle atrophy, we performed mRNA sequencing of quadriceps from *Bcl6*$^{i\text{-MKO}}$ mice 1 week after tamoxifen-induced *Bcl6* deletion. Our analysis revealed 3,595 differentially expressed (DE) genes compared to corn oil-treated *Bcl6*$^{i\text{-MKO}}$ controls (Cre^{+} oil) or 2,592 genes compared to tamoxifen-treated *Bcl6*$^{fl/fl}$ controls (Cre^{-} tmx; Fig. 5a). Despite some tamoxifen-driven contributions to gene expression variance (Extended Data Fig. 5a), 2,114 DE genes were identified between knockouts and both oil-treated and tamoxifen-treated controls, with 2,103 high-confidence genes exhibiting strongly correlated expression changes (r_s = 0.96; Fig. 5b). Prior studies have suggested a role for BCL6 to oppose STAT proteins, particularly STAT5 (refs. 26,27). However, we detected only 79 genes in common between our high-confidence muscle *Bcl6* DE gene set and published microarray data from muscle-specific *Stat5*-knockout mice (Extended Data Fig. 5b)[28]. This corresponded to only 13% of STAT5-regulated genes and 4% of BCL6-regulated genes, respectively, and we found no correlation in their regulation (Extended Data Fig. 5c). These findings suggest that BCL6 controls a distinct muscle gene network.

Ontology analysis of our high-confidence BCL6-regulated gene set identified top scoring terms of translation, ribosome biogenesis and assembly, muscle structure development, modification by small-protein conjugation, and striated muscle contraction (Fig. 5c). Within these varied categories, we found many well-documented regulators of muscle structure and proteostasis (Fig. 5d). In line with the slow myofibre enrichment in *Bcl6*-knockout tissue, transcript levels for myosin light and heavy chains and troponins (*Myl2*, *Myl6b*, *Myh2* and *Tnni1*) were increased, and contraction-related genes encoding components of the sarcoplasmic reticulum (*Sln*, *Casq2*) and Z-disc (*Ky*) were elevated and reduced, respectively. Expression of key signalling components controlling muscle mass including myostatin (*Mstn*) and growth arrest and DNA damage-inducible alpha (*Gadd45a*) were increased, while anabolic genes including androgen receptor (*Ar*) and IGF-1 (*Igf1*) were decreased. The genes encoding critical translation inhibitor (*Eif4ebp1*), ribosome components (*Rpl9*, *Rps28*) and RNA binding proteins like *Zfp36l1* and *Cirbp* were strongly induced in *Bcl6*-ablated muscle, while RNA binding proteins like Cpeb1 implicated in translational initiation were reduced[29–34]. In addition, genes encoding synthetic enzymes for spermidine and spermine (*Amd1/Amd2*, *Smox*), which are essential polycations required for translation, were reduced in *Bcl6*-deleted muscle[35,36]. Finally, *Bcl6* ablation also elevated the levels of many ubiquitin ligases including *Cul7* and *Rnf217*, and decreased the levels of deubiquitinases like *Usp13* and *Usp44*. Together, these transcriptional changes suggested the potential for *Bcl6* to control muscle mass and function through multiple molecular targets influencing protein synthesis and breakdown.

BCL6 has been characterized as a transcriptional repressor in immune cells, liver and adipose tissue[18,37,38], but its direct regulatory impact in skeletal muscle has not been established. To further address its epigenomic control, we performed BCL6 ChIP–seq in C57BL/6 mouse quadriceps. Using a stringent false discovery rate (FDR) cutoff of 1×10^{-7}, we identified 10,925 BCL6 binding peaks, over 88% of which were promoter-distal binding in location (Fig. 5e). Motif analysis of these sites showed a striking enrichment

of consensus recognition sequences for BCL6 (Fig. 5f) and, to a lesser extent, motifs for well-known muscle transcription factors including MEF2 and SIX. Top ontologies for nearby genes included muscle development and adaptation, actomyosin structure and translation (Fig. 5g). Moreover, mouse phenotypes associated with genes vicinal to BCL6 peaks included decreased skeletal muscle fibre size, impaired contractility and muscular atrophy, recapitulating the phenotype of mice lacking skeletal muscle *Bcl6* (Fig. 5g). BCL6 is known to interact with many corepressors including HDAC3 (refs. 37,39). To test whether loss of BCL6 affects acetylation in skeletal muscle, we performed ChIP–seq for H3K27ac in Cre^{-} tmx and $Bcl6^{i\text{-}MKO}$ mice following tamoxifen treatment and detected significantly more signal surrounding BCL6 binding sites in knockout muscles, with an overall 15% increase in H3K27ac within 1 kb of peak centres (Extended Data Fig. 5d).

Next, we integrated our RNA-seq and BCL6 ChIP–seq datasets using the Cistrome-GO pipeline to determine putative direct targets for BCL6 and define its regulatory potential[40]. Interestingly, we found that among genes that were transcriptionally altered by muscle *Bcl6* ablation and located in the vicinity of BCL6 binding sites, BCL6 could act both as a transcriptional activator and repressor (Extended Data Fig. 5e). However, there was a stronger association with gene repression (that is, upregulated expression in *Bcl6*-ablated muscle) than activation. Both negative and positive transcriptional regulation were apparent among putative direct target genes of BCL6 (Fig. 5h). For example, BCL6 was predicted to repress *Eif4ebp1* and *Mstn* but activate the expression of *Igf1* and *Ar*. To further confirm direct BCL6 target genes, we performed nascent RNA-seq in vivo using 5-ethynyluridine labelling while acutely exposing mice to FX-1. a selective BCL6 inhibitor that competes off its corepressor interactions with SMRT, NCoR and BCoR[41]. This nascent RNA-seq data revealed that *Eif4ebp1* is induced within 3 h of BCL6 inhibition, while *Igf1* and *Ar* are simultaneously suppressed (Fig. 5i). In contrast, *Mstn* expression was unchanged, indicating either indirect BCL6 regulation or direct BCL6 regulation mediated via corepressors that are not targeted by FX-1. Gene-level visualization of our mRNA and nascent RNA-seq data confirmed that the expression of *Eif4ebp1* and *Mstn* was increased and the expression of *Igf1*, *Smox* and *Ar* was decreased in *Bcl6*-deleted muscles (Fig. 5j and Extended Data Fig. 5f). Moreover, BCL6 binding sites were present in the vicinity of these genes, and there were changes in the surrounding H3K27ac signals that parallelled alterations in gene transcription. These findings suggested a target-specific role for BCL6 to directly repress or activate genes controlling muscle proteostasis.

The atrophy and loss of strength caused by *Bcl6* muscle deletion appeared relatively more modest in females than in males (Extended Data Figs. 2b,d and 4a,b), raising the possibility that *BCL6* gene regulation could be sexually dimorphic in muscle, as has been reported for its regulation in the liver[26]. We found that in $Bcl6^{fl/fl}$ control animals, muscle levels of *Bcl6* transcript were significantly lower and BCL6 protein trended lower in females than males (Extended Data Fig. 5g,h). Accordingly, the transcriptional impact of BCL6 on both repressed targets (*Akt1*, *Eif4ebp1*) and activated targets (*Igf1*, *Ar*) was less robust in females compared to males, although most of these target genes were still significantly altered in muscle *Bcl6*-deleted females (Extended Data Fig. 5g). These results indicated that BCL6 has an attenuated transcriptional impact in the muscle of females.

BCL6 promotes skeletal muscle protein synthesis

Conditions that cause muscle atrophy perturb the balance between protein synthesis and degradation in varying ways. For example, starvation and cancer cachexia reduce protein synthesis and increase protein degradation by both autophagy and the proteasome, whereas nerve injuries increase protein synthesis but more profoundly increase degradation[42–44]. To address how loss of *Bcl6* led to reduced muscle mass, we performed deuterium labelling in $Bcl6^{i\text{-MKO}}$ and control mice using a non-steady-state precursor labelling strategy that we have previously validated for determining protein turnover rates in vivo[45,46]. One week after tamoxifen administration, a bolus of deuterated saline was administered and $Bcl6^{i\text{-MKO}}$ and $Bcl6^{fl/fl}$ control mice were serially collected over the course of a week. Collected tissues were used to determine ^{2}H-labelling of protein-bound alanine in muscle by gas chromatography–mass spectrometry (GC–MS) as well as relative alanine concentrations. Skeletal muscle-bound alanine levels were significantly reduced in $Bcl6^{i\text{-MKO}}$ mice compared to Cre^{-} tmx controls 2 d after deuterium labelling (Fig. 6a). Furthermore, isotope kinetics were analysed with a mathematical model to determine absolute protein synthesis rates, which identified a 26% reduction in protein synthesis among muscle *Bcl6*-deleted animals (Fig. 6a). To confirm results from our deuterium studies, we further tested protein synthesis in skeletal muscle *Bcl6*-ablated animals. We used surface sensing of translation (SUnSET) to determine protein synthesis based on acute puromycin incorporation into elongating peptides in skeletal muscles[47] and compared tamoxifen-treated $Bcl6^{i\text{-MKO}}$ with Cre^{-} tmx mice. Western blotting with anti-puromycin revealed 54% reduced puromycin incorporation into *Bcl6*-ablated muscles compared to controls (Fig. 6b).

Next, we crossed $Bcl6^{i\text{-MKO}}$ mice to animals encoding HA epitope-tagged ribosomes (RiboTag mice) and generated tamoxifen-inducible muscle ribosome-tagged *Bcl6* knockouts ($Bcl6^{i\text{-MKO}}$ *mRiboTag*) and controls (*mRiboTag*) to test the impact of *Bcl6* on translation using ribosome profiling (Fig. 6c)[48]. Muscle lysates were treated with T1 RNase and ribosomes were immunoprecipitated to isolate ribosome protected fragments (RPFs). Over two-thirds of the recovered RPFs were between 26 and 30 nucleotides, and over 82% of RPFs mapped to coding DNA sequences in both the $Bcl6^{i\text{-MKO}}$ *mRiboTag* and control samples (Extended Data Fig. 6a,b). Remarkably, Ribo-seq revealed that more than three times as many genes were significantly altered at the translational level than at the transcriptional level in *Bcl6*-ablated muscle (Fig. 6d). We detected a significant (P value $< 2.2 \times 10^{-16}$) overall reduction in translation efficiency (TE; Extended Data Fig. 6c) with 1,887 translating mRNAs significantly reduced and 1,203 translating mRNAs enhanced following *Bcl6* deletion (Fig. 6e). Moreover, we found that the distribution of RPFs was increased in the vicinity of the translation start site (TSS) but decreased along protein coding sequences in $Bcl6^{i\text{-MKO}}$ *mRiboTag* muscle, particularly among TE-reduced mRNAs (Fig. 6f and Extended Data Fig. 6d). TE-reduced targets were enriched for functions in extracellular matrix, vascular development, locomotion and cell adhesion (Fig. 6g), including laminin subunit gamma 1 (*Lamc1*) and collagen 1a1 (*Col1a1*; Fig. 6h). In contrast, TE-enhanced transcripts encoded proteins associated with nuclear bodies, mRNA processing, ribonucleoprotein complexes, chromatin binding and protein catabolism (Fig. 6g). Among these TE-enhanced mRNAs were transcripts with various roles in autophagy including initiation signalling (*Cisd2*, *Rab12*), ubiquitin-mediated cargo selection (*Rnf166*),

mitophagy (*Fundc1*, *Rnf166*), ATG conjugation (*Atg3*), the lysosome (*Ubqln1*, *Ubqln4*, *Rab1b*, *Rab24*) and membrane delivery (*Supt20h*). Together, these findings reveal an extensive role for BCL6 to support translation beyond its immediate impact on transcription.

We also tested whether protein degradation was altered by loss of muscle *Bcl6*. We first assessed for changes in ubiquitin-mediated proteolysis by measuring ubiquitin signals in muscle lysates from *Bcl6*-ablated and control mice. We observed no changes in ubiquitin after *Bcl6* deletion when examined 10 d (Extended Data Fig. 6e) or at later times after tamoxifen treatment. We interrogated autophagy using western blotting after treating both Cre^{-} tmx and $Bcl6^{i\text{-}MKO}$ mice (10 d after tamoxifen treatment) with either vehicle or colchicine, a drug that blocks autophagosome degradation[49,50]. While colchicine caused accumulation of LC3-II levels in both Cre^{-} tmx and $Bcl6^{i\text{-}MKO}$ muscles, flux analysis indicated higher rates of autophagy in $Bcl6^{i\text{-}MKO}$ mice (1.7 fold higher than controls; Fig. 6i). Collectively, these findings indicated that acute atrophy from skeletal muscle deletion of *Bcl6* was attributable to reduced protein synthesis and increased autophagy.

BCL6 controls 5′ mRNA cap-dependent translation initiation

Accumulation of ribosomes at the start codon and corresponding depletion of ribosomes towards the stop codon indicated a defect in translation initiation in $Bcl6^{i\text{-}MKO}$ *mRiboTag* muscles (Fig. 6f). Consistent with a role for BCL6 in cap-dependent translation initiation, we observed 5′ terminal oligopyrimidine (TOP) tracts among TE-reduced mRNAs but none in TE-upregulated transcripts (Fig. 6e). Based on these observations, we next sought to understand the molecular basis for reduced translation initiation in muscle *Bcl6*-ablated mice. A major regulatory step in cap-dependent translation initiation is the binding of 4EBP1 to EIF4E, which represses protein synthesis by blocking interaction between EIF4G and EIF4E (Fig. 7a). Using co-immunoprecipitation and western blotting to measure the EIF4E-associated proteins, we detected a clear increase in the inhibitory 4EBP1–EIF4E complex along with a corresponding decrease in the interaction of EIF4G with EIF4E in $Bcl6^{i\text{-}MKO}$ muscle (Fig. 7a and Extended Data Fig. 6f). Given the critical role of threonine phosphorylation in modulating 4EBP1 activity, the above observation may result from enhanced 4EBP1 expression or reduced phosphorylation. Western blots to measure the levels of 4EBP1 and Thr37/Thr46 phosphorylation demonstrated a significant increase in 4EBP1 accompanied by a similar boost in p4EBP1 (Fig. 7b). Most importantly, we also tested levels of non-phosphorylated 4EBP1, the form that inhibits EIF4E. We observed significantly increased levels of non-phosphorylated 4EBP1 in $Bcl6^{i\text{-}MKO}$ mice (Fig. 7b), consistent with the reduced muscle protein synthesis observed following *Bcl6* ablation. Similar results were obtained in western blot experiments of 4EBP1 in muscle lysates from constitutive $Bcl6^{MKO}$ mice (Extended Data Fig. 6g). These observations indicated that BCL6 promotes translation by suppressing 4EBP1.

We next tested how BCL6 controls the eIF4E–4EBP1 axis and convergent signalling cascades. Our ChIP–seq and RNA-seq experiments predicted a direct regulatory role for BCL6 on *Eif4ebp1*, *Akt1*, *Igf1*, *Ar*, and possibly *Mstn* (Fig. 5h–j and Extended Data Fig. 5f). We confirmed increased muscle expression of *Eif4ebp1* and *Mstn* as well as suppressed *Ar* and *Igf1* using qPCR (Extended Data Fig. 6h). Protein levels of muscle

myostatin were almost 60% higher in *Bcl6*$^{i\text{-MKO}}$ mice than in controls (Fig. 7c). Conversely, we detected a greater than twofold reduction of AR protein in *Bcl6*-deleted muscle (Fig. 7c). To address the signalling impact of reduced *Igf1* and AR in *Bcl6*-ablated muscle, we interrogated total and phosphorylated levels of AKT and its downstream signalling targets S6 and FOXO1. Total AKT protein was significantly increased in *Bcl6*-knockout tissue (Fig. 7d), consistent with our observation that *Akt* is a directly repressed BCL6 skeletal muscle target gene (Fig. 5i). Active, phosphorylated AKT (Ser473) levels were also increased (Fig. 7d), but phosphorylated forms of S6 (Ser 240/Ser244; Fig. 7d) and FOXO1 (Ser256) were significantly lower (Fig. 7d). Finally, we interrogated SMAD proteins, which transduce signals from transforming growth factor beta superfamily members including myostatin and modulate AKT–mTORC1 signalling[7]. We could not detect phosphorylated SMAD2/SMAD3 in muscle lysates from tamoxifen-treated *Bcl6*$^{i\text{-MKO}}$ or control mice, but levels of the pro-anabolic regulator phospho-SMAD1/SMAD5/SMAD8 trended lower ($P = 0.07$) in *Bcl6*-knockout tissues (Fig. 7e)[51,52]. These results indicated complex changes along the IGF–AKT–mTORC1 axis with loss of *Bcl6* that at one level could be pro-anabolic (for example, increased phospho-AKT), yet downstream signalling was pro-atrogenic (for example, reduced phospho-S6 and phospho-FOXO1).

Finally, we tested the functional impact of 4EBP1 on muscle atrophy in *Bcl6*-deleted mice. We developed MyoAAV4A vectors encoding *Eif4ebp1* shRNAs or a scramble negative control[53]. We infected mice with viruses and 1 week later treated all animals with tamoxifen to delete *Bcl6* in *Bcl6*$^{i\text{-MKO}}$ animals or serve as a drug control in *Bcl6*$^{fl/fl}$ mice. Skeletal muscles were collected 8 weeks later. We found that our two *Eif4ebp1* shRNAs knocked down *Eif4ebp1* transcripts by 50–73% and corresponding protein levels by 20–40% in *Bcl6*-deleted skeletal muscles (Extended Data Fig. 6i,j). Remarkably, *Bcl6* muscle knockout myofibre CSAs increased by 35–64% in mice with reduced 4EBP1, partially rescuing the atrophy observed in *Bcl6*$^{i\text{-MKO}}$ mice (Fig. 7f). These observations highlight a key role for BCL6-mediated regulation of *Eif4ebp1* and signalling pathways that converge with the IGF–AKT–mTORC1 axis to control translation and muscle mass (Fig. 8)[54].

Chronic *Bcl6* loss evokes compensation to maintain muscle

While inducible deletion of *Bcl6* caused acute muscle atrophy, lean mass became relatively stable after ~6 weeks (Fig. 2d and Extended Data Fig. 2a,b). To understand this compensation, we examined protein synthesis and degradation in *Bcl6*$^{i\text{-MKO}}$ mice after 12 weeks of *Bcl6* deletion. In contrast to the early effects of *Bcl6* deletion that reduced protein synthesis (Fig. 6a,b), chronic deletion led to a modest increase in overall protein synthesis based on puromycin incorporation (Extended Data Fig. 7a). In addition, we observed slightly more autophagic flux in *Bcl6*-ablated muscles (Extended Data Fig. 7b), but these effects were more modest than the increase observed immediately after *Bcl6* deletion (Fig. 6i). Finally, we examined ubiquitin-dependent proteolysis by blotting for ubiquitinated proteins, but we detected no change between genotypes (Extended Data Fig. 7c), mirroring findings at earlier timepoints after *Bcl6* deletion. Thus, chronic adaptation for loss of *Bcl6* involves raising protein synthesis and attenuating autophagy to preserve muscle mass.

To understand the molecular mechanisms of compensation from *Bcl6* deficiency, we analysed gene regulatory and signalling changes that distinguish chronically from acutely *Bcl6*-deleted muscles. First, we performed mRNA-seq and detected nearly 1,300 gene expression changes unique to chronically *Bcl6*-deleted tissue (Extended Data Fig. 7d). Gene Ontology (GO) analysis for these altered transcripts revealed regulation of TOR signalling and negative regulation of cellular catabolism among top scoring terms (Extended Data Fig. 7e). Next, we carried out ChIP–sequencing of acetylated H3K27, a marker for enhancer and promoter activity, to find epigenomic changes associated with chronically *Bcl6*-deleted muscles. We analysed our mRNA-seq and H3K27ac ChIP–seq datasets from acute and chronic *Bcl6* deletion using Integrated analysis of Motif Activity and Gene Expression (IMAGE)[55]. This machine learning analysis identified many putative causal transcription factor motifs that were either (1) uniquely associated with gene transcription in acute or chronic *Bcl6* deletion, or (2) commonly associated with gene transcription in both acute and chronic *Bcl6* deletion but with opposite correlations to expression at these two times. Among the unique associations, motifs for NR4A nuclear receptors, which have been implicated in exercise performance and muscle mass, were predicted with highest confidence to be causal (Extended Data Fig. 7f)[56,57]. Motifs for KLF, NKX, PBX and ZBTB factors were also predicted to contribute to time of *Bcl6* deletion-dependent transcription with a modest degree of confidence and, to a lesser extent, FOXO transcription factors (Extended Data Fig. 7f). Motifs with opposing correlations to gene expression in acutely versus chronically *Bcl6*-deleted muscles included members of the KLF, MEF, MYOG, ZKSCAN (TFEB) and SMAD families, among several others (Extended Data Fig. 7g). Consistent with our GO and motif prediction analyses, we detected increased pro-anabolic phospho-SMAD1/SMAD5/SMAD8 signalling in chronically *Bcl6*-deleted muscles (Extended Data Fig. 7h). Additionally, we found that phosphorylated FOXO1, which was acutely reduced by *Bcl6* deletion (Fig. 7d) was restored in knockouts 12 weeks later (Extended Data Fig. 7i), possibly mitigating the atrophy programme directed by its non-phosphorylated form. Profiles of phosphorylated and total levels of AKT, 4EBP1 and S6 in chronically *Bcl6*-ablated muscles resembled those observed immediately after *Bcl6* deletion (Extended Data Fig. 7j–l). Overall, these findings pointed to a network of epigenomic regulators that redirected transcription and cell signalling to attenuate muscle loss from chronic *Bcl6* deficiency by restoring protein synthesis and reducing catabolism.

Discussion

After nearly 30 years since the cloning and initial description of *BCL6* as a proto-oncogene highly expressed in normal adult skeletal muscle[10], we have discovered a potent regulatory role for BCL6 in the acquisition and maintenance of muscle mass and strength. We identified multiple anabolic regulators as direct BCL6 targets using genome-wide mRNA-seq, nascent RNA-seq and DNA binding analyses, including both directly BCL6-repressed targets such as *Eif4ebp1* and BCL6-activated targets such as *Igf1* and *Ar*. We postulate that de-repression of 4EBP1 and attenuated anabolic signalling driven by IGF-1, AR and SMAD pathways cause translational defects in *Bcl6*-ablated muscle. These effects are attributable, at least in part, to impaired cap-dependent translation, as evidenced by reductions in cellular EIF4G–EIF4E complexes, reduced ribosome occupancy across the coding sequences of

thousands of genes, and partial rescue of myofibre atrophy with *Eif4ebp1* knockdown in *Bcl6*-ablated skeletal muscle.

We found that BCL6 controls both the protein synthetic and degradative arms of muscle proteostasis. Based on ribosomal sequencing, BCL6 regulates the translation of many contractile proteins, which are among the most abundant in muscle, and vascular and remodelling factors that participate in the control of tissue differentiation and mass[58,59]. It also directs translation of extracellular matrix components, including collagens and laminins implicated in muscular dystrophies. Although dystrophic changes were not apparent in *Bcl6*-deleted muscle, these findings suggest that BCL6 could be relevant in other muscle pathologies. Additionally, we identified a role for BCL6 in the suppression of autophagy in skeletal muscle, as we observed increased autophagic flux in mice after *Bcl6* deletion. However, changes in the expression of autophagy-related genes were only modest in magnitude in knockout muscles, suggesting that BCL6-mediated control of autophagy may occur through a post-transcriptional mechanism. Indeed, our ribosomal sequencing data indicated that BCL6 suppresses the translational efficiency of proteins with varied functions in autophagy and raises the intriguing possibility that translational control underlies its regulation of autophagy. While de-repression of *Eif4ebp1* is a likely candidate for initiating translational changes in our *Bcl6* deletion models of muscle atrophy, the importance of other BCL6 targets linked to anabolic regulation is unknown. Precisely defining the effects of the IGF-1–AKT–mTOR pathway, SMAD, and androgen-induced signalling on skeletal muscle translation in vivo will be key to further frame our findings for BCL6 and understand the extent to which these pathways converge in their control of proteostasis.

Skeletal muscle atrophy frequently occurs in a fibre-type-specific manner and is accompanied by shifts in muscle myofibre composition, although mechanisms underlying these observations are incompletely understood[24,25]. Atrophy from denervation or immobilization, for example, primarily affects type 1 fibres and is associated with a switch from slow to fast myofibres. Conversely, atrophy from cancer, sepsis, diabetes or aging is more pronounced in type 2 fibres and is linked to transition from fast to slow fibres. Resembling these illness-related and nutrient-related conditions, *Bcl6* ablation leads to atrophy in predominantly glycolytic myofibres and promotes a shift to a slower myosin heavy chain isoform composition. Interestingly, this shift was not associated with altered mitochondrial content or fatigability in *Bcl6*-deleted muscles, consistent with other reports in which fibre type and mitochondrial metabolism can become disassociated[60]. Furthermore, we observed marked reductions of muscle BCL6 in starvation and cancer cachexia models, and we found that BCL6 suppresses slow fibre-associated *Myh2* and *Myh7b* but activates fast fibre-associated *Myh4*. These findings suggest that, in addition to a developmental role, BCL6 directs an integrated transcriptional programme controlling translation and myofibre specification in muscle wasting. The extent to which muscle BCL6 controls atrophy in pathophysiological states, particularly in humans, warrants further investigation.

Transcriptional repressors and corepressors play key roles in the regulation of muscle mass and metabolism. Despite documented physical interactions with NCoR1 and class II HDACs, which suppress muscle mass[15,61,62], we discovered an anabolic role for BCL6. Surprisingly, our integrated ChIP–seq and RNA-seq analyses suggested potential for BCL6

in muscle to function not only as a repressor but also as a gene-specific activator of transcription. These observations indicate BCL6 may engage alternative cofactor complexes to direct transcription in muscle, as has been described in B cells[37]. It is also notable that previous studies have suggested opposing roles for BCL6 and STAT5 in the regulation of gene expression and involvement for both pathways in liver sex-specific transcription[11,26,27]. Yet muscle-specific deletion of STAT5 resulted in skeletal muscle atrophy resembling the phenotype we observed in mice lacking muscle *Bcl6* (ref. 28), and we found no correlation between gene expression changes in *Bcl6*-ablated and *Stat5*-ablated skeletal muscles. Consistent with its male-biased regulation in liver, we found that the transcriptional and functional impact of *Bcl6* deletion on muscle mass and strength was more profound in males than in females. The basis for these sex differences is likely multifaceted, but reduced BCL6 and constitutively elevated 4EBP1 levels in female muscle are likely contributors (Extended Data Fig. 5h,i). Collectively, our findings establish a role for BCL6 in skeletal muscle protein homeostasis and contribute to an expanding recognition for BCL6 as a sexually dimorphic regulator of metabolism outside the immune system[18,38].

Methods

Animals

All strains were in the C57BL/6 genetic background. $Bcl6^{fl/fl}$ mice[18] were crossed with HSA-Cre mice (JAX, 006149) to generate $Bcl6^{fl/fl}$;HSA-Cre ($Bcl6^{MKO}$) mice. $Bcl6^{fl/fl}$ mice were also crossed with animals expressing Cre fused to two mutated oestrogen receptors driven by the HSA promoter (JAX, 025750), to generate animals for tamoxifen-inducible *Bcl6* deletion in muscle ($Bcl6^{i\text{-}MKO}$ mice). Tamoxifen-inducible muscle ribosome-tagged *Bcl6* knockouts ($Bcl6^{i\text{-}MKO}$ *mRiboTag*) and controls (*mRiboTag*) were generated by further crossing $Bcl6^{i\text{-}MKO}$ mice and controls to RiboTag mice (JAX, 011029). To induce *Bcl6* deletion or expression of HA-tag on muscle ribosomes, 8- to 12-week-old mice were treated with tamoxifen (75 mg per kg body weight; Sigma, T5648) for four consecutive days via intraperitoneal injections. C57BL/6J (000664) mice were purchased from the Jackson Laboratory. All mice were maintained on a 14-h–10-h light–dark cycle with free access to standard chow and water at temperatures of 21–23 °C with 30–70% humidity. All animal care and use procedures were conducted in accordance with regulations of the Institutional Animal Care and Use Committees at Northwestern University and the Jesse Brown VA Medical Center under protocols IS00000321, IS00005071, IS00016185 and BX004898.

In vitro models

For primary myoblast culture, limbs were dissected from newborn C57BL/6J mice (postnatal day 1–3), washed in PBS, minced and incubated in 0.2% Collagenase D (Roche, 11088882001) solution (1 ml/0.3 g of muscle) for 30–45 min at 37 °C. The slurry was triturated every 10–15 min and filtered into a 50-ml conical tube through a 100-μm filter by adding the slurry followed by 10 ml PBS and 5 ml F10-Ham's media (Thermo Fisher, 11550–043) with 20% FBS (Thermo Fisher, 11550), 1% Anti-Anti (Thermo Fisher, 15240–062) and 2.5 ng ml^{-1} bFGF (Promega, G5071). The filtered cells were then grown on 60-mm plates coated with ECL (Sigma, 08110) at 37 °C with 8% CO_2. Once cells reached

80–90% confluence, they were differentiated in DMEM (Life Technologies, 11965–084) medium with 2% horse serum and 1% Anti-Anti with medium changes every 12 h for 5 d.

Colon-26 cells (American Type Culture Collection, CRL-2638) were grown to confluence in 10-cm plates using DMEM media supplemented with 10% FBS. Confluent cells were washed with PBS, and medium was replaced with DMEM supplemented with 2% horse serum for 26 h. Conditioned medium was collected, sterilized with a 22-μm filter, and added to C2C12 myotubes to a concentration of 33% conditioned medium.

Differentiated C2C12 myotubes were exposed to dexamethasone (1 μM, Sigma), growth hormone (500 ng ml^{-1}), IL-6 (100 pg ml^{-1}; PeproTech), tumour necrosis factor (10 ng ml^{-1}; PeproTech), IL-1β (10 ng ml^{-1}, PeproTech) and STAT3 inhibitor galiellalactone (10 μM; Cayman Chemical).

Body composition, muscle weight measurements and activity

Body composition was determined using magnetic resonance imaging (EchoMRI 2014 Body Composition Analyzer v.140320). For *Bcl6*$^{i\text{-MKO}}$ mice, body composition was analysed weekly or biweekly beginning just before tamoxifen treatment to progressively monitor the effects of *Bcl6* deletion. At experimental endpoints, muscles were isolated and weighed. Mouse activity was measured using the Phenomaster Caging System (TSE Systems) with infra-red sensors.

Histology

For paraffin-embedded sections, muscles were fixed in 10% formalin (Fisher, 245–684) overnight and transferred to 70% ethanol. Further processing and H&E staining was performed at Northwestern University's Mouse Histology and Phenotyping Laboratory. For frozen sections, muscles were embedded in OCT compound (Tissue-Tek, 4583) and cut with 10-μm transverse sections taken from three regions at mid-body at least 150 μm apart. Muscle sections were fixed with ice-cold acetone and incubated in blocking solution (10% FBS, 0.1% Triton X-100 in 1× PBS) for 1 h at room temperature. Primary antibodies were added and incubated overnight at 4 °C. The following dilutions of mouse monoclonal antibodies from Developmental Studies Hybridoma Bank were used for fibre-type staining: MYH7/BA-F8—type I (1:10 dilution), MYHIIA/SC-71—type 2 A (1:30 dilution) and MYH/IIB/BF-F3—type 2B (1:10 dilution). Rabbit anti-laminin from Sigma-Aldrich (L9393; 1:1,000 dilution) was used to delineate fibre borders. The next day, slides were incubated with secondary antibodies for 1 h at room temperature, washed and mounted with Prolong Antifade Diamond (Thermo Fisher, P36970). Slides were imaged on a Zeiss Axio bright-field or Keyence BZ-X810 fluorescence microscope. Muscle myofibre CSA was calculated from H&E images using Image Pro software v9.2 (Media Cybernetics) or laminin immunofluorescence (Sigma-Aldrich, L9393) using Keyence BZ-X810 software. Areas were determined for at least 800 cells per mouse.

Muscle function analysis

Forelimb strength was measured using a grip strength meter (Columbus instruments, 1027SM). Mice were given three trials, with 5 s rest on a flat surface between pulls.

The maximum of the three readings was used. In situ tetanic force from TA muscles was measured using a Whole Mouse Test System (Aurora Scientific, 1300 A) with a 1 N dual-action lever arm force transducer (Aurora Scientific, 300C-LR) in anaesthetized animals (3% isoflurane in 100% O_2). Parameters for tetanic isometric contractions were as follows: initial delay, 0.1 s; frequency, 200 Hz; pulse width, 0.5 ms; duration, 0.5 s; and stimulation, 100 mA. Length was adjusted to a fixed baseline of 30 mN resting tension for all muscles. Specific force was calculated by normalizing maximum force to the CSA. Treadmill experiments were run on an Exer 3/6 Treadmill (Columbus Instruments International) at 10-degree inclines. Animals were acclimated by running at 1 m min^{-1} for 2 min after which speed was increased every minute by 1 m min^{-1} until exhaustion. Time to exhaustion was determined as the time at which an animal no longer kept pace with the belt and received ten shocks in 1 min.

Protein isolation and quantification

Cells were dounce homogenized in cold RIPA buffer consisting of 1 mM EDTA (Sigma, E9884), 0.5 mM EGTA (Sigma, E4378), 1% Triton X-100 (Sigma, T8787), 0.1% sodium deoxycholate (Sigma, D6750), 0.1% SDS (Sigma, L3771), 140 mM NaCl (Sigma, S9888) and protease (Roche, 05892970001) and phosphatase (Roche, 04906837001) inhibitors. Snap-frozen tissues were homogenized in cold SDS lysis buffer consisting of 50 mM Tris pH 7.5 (Teknova, T1075), 100 mM NaCl, 1 mM EDTA, and protease (Roche, 05892970001) and phosphatase (Roche, 04906837001) inhibitors using a Qiagen Tissue-Lyser. Samples were spiked with 0.5% SDS, and they were rotated for 15 min at 4 °C. Protein was collected by centrifugation at >12,000*g* for 15–20 min and quantified using BCA assays (Thermo Fisher) measured at 562 nm using a SpectraMax Plus spectrophotometer (Molecular Devices).

Western blotting

Protein lysates were denatured by heat treatment and separated in 4–20% or Any kD TGX Precast Gels (Bio-Rad, 4568094 or 4569034). For OxPhos blots, non-denatured protein lysates were applied to a 16.5% Tricine gel. For LC3 blots, protein lysates were applied to 12% TGX Precast Gel (Bio-Rad, 4561043). Gels were transferred to 0.2-μm PVDF membranes (Bio-Rad, 1704157) and stained with 0.2% Ponceau S (Sigma, P3504) solution to assess transfer efficiency before blocking in 5% milk (Bio-Rad, 1706404) in 1× PBS with 0.1% Tween 20 (PBST; Teknova, P2192) or Intercept Blocking Buffer (LI-COR, 927–60001) followed by overnight primary antibody incubation at 4 °C. Primary antibodies were diluted in 5% BSA (Bio-Rad, 1706404) in 1× PBST or Intercept T20 Antibody Diluent (LI-COR, 927–65001) at 1:1,000 dilution unless otherwise indicated for western blots. The following primary antibodies were used: α-phospho-AKT Ser473 (4060), α-Pan-AKT (4691), α-LC3 A/B (12741), α-phospho-4EBP1 Thr37/Thr46 (2855), α-non-phospho4EBP1 Thr46 (4923), α−4EBP1 (9644), α-eIF4G (2469), α-phospho-S6 Ser240/Ser244 (5364), α-total S6 (2217), α-phospho-FOXO1 Ser256 (9461), α-FOXO1 (2880), α-ubiquitin (3936), α-SMAD1 (6944, Cell Signaling), α-phospho-SMAD1/SMAD5/SMAD8 (Vli31, MaineHealth Institute for Research; 1:2,000 dilution), α-Myostatin (ab98337; 1:250 dilution), AR (ab108341), VDAC (ab15895, AbCam), α-BCL6 (7388), α-eIF4E (2067, Santa Cruz Biotechnology), α-Actin (A2066), α-Tubulin

(T4026; Sigma-Aldrich), α-puromycin (PMY-2A4; Developmental Studies Hybridoma Bank; 1:500 dilution) and OxPhos Rodent WB Antibody (45–8099; Thermo Fisher; 1:250 dilution). After the overnight incubation, blots were washed and incubated with horseradish peroxidase-conjugated secondary antibodies (Jackson ImmunoResearch, 115–035-174 and 211–032-171) at 1:10,000 dilution for 1 h, and visualized on a Protein Simple FluorChem E v5.0.4 or LI-COR Fc digital imager v5.2 using enhanced chemiluminescent horseradish peroxidase substrate (Thermo Fisher SuperSignal West Pico Plus, 34577). Multiple targets were probed on the same blot by stripping with OneMinute Advance Western Blot Stripping Buffer (GM Biosciences, GM6031) before adding a different primary antibody. Memcode Reversible Stain (Thermo Fisher, 24585) or Revert 700 Total Protein Stain (LI-COR, 926–11016) was used to visualize total protein. Protein densitometry was quantified using ImageJ 1.51s.

Immunoprecipitation

Muscles were collected, snap frozen and dounced ~10× in lysis buffer containing 50 mM Tris-HCl, 150 mM NaCl,1% NP40 (Igepal, CA-630) and 0.5% sodium deoxycholate. After mixing at 4 °C, lysates were spun down, and supernatants were collected. For immunoprecipitations, 3 μg of eIF4E antibody (Santa Cruz, 271480) or mouse IgG antibody (Santa Cruz, 2025) were added to 750 μg of protein lysate and rotated overnight at 4 °C. The following day, antibody complexes were precipitated with 50 μl of protein G beads and washed four times with 0.1 M sodium phosphate containing 0.01% Tween and cOmplete EDTA-free protease inhibitors (Sigma). Protein complexes were eluted for western blotting using 35 μl of 2× loading buffer and boiled for 10 min.

RNA and DNA isolation and qPCR

For RNA extraction, snap-frozen tissues were homogenized in TRIzol (Thermo Fisher, 15596018) using a MoBio Powerlyzer 24 and incubated with chloroform (Sigma, C2432). RNA was isolated using RNeasy kits (Qiagen, 74106) and used for qPCR or next-generation sequencing. For qPCR, RNA was quantified using a Nanodrop spectrophotometer (ND-1000) and cDNA was synthesized using iScript cDNA synthesis kits (Bio-Rad, 170–8891). Real-time qPCR was performed with SYBR Green Master Mix (Bio-Rad, 1725124) on a Bio-Rad CFX384 Touch Real-Time PCR System and analysed using Bio-Rad CFX manager software v3.1 (184500). RNA expression was determined using the relative standard curve method and normalized to the housekeeping gene *36b4*. For nuclear and mitochondrial DNA isolation, muscles were processed using DNeasy kits (Qiagen). The mitochondrial DNA/nuclear DNA ratio was calculated as the ratio of *Cytb* or *Cox1* to *Gcg* or *Hbb* as determined by ΔΔCt method. Primer sequences are listed in Supplementary Table 1.

mRNA sequencing and analysis

RNA quality was assessed using a Bioanalyzer RNA 6000 nano kit (Agilent, 5067–1511) to ensure RNA Integrity Number scores > 7.0. Sequencing libraries were constructed using TruSeq Stranded mRNA sample prep kits (Illumina, 20020594) and quantified using Bioanalyzer High Sensitivity DNA kit (Agilent, 5067–4627) and qPCR (Kapa Biosystems, KK4824) and sequenced on Illumina NextSeq 500 and 2000 or HiSeq 4000 instruments.

RNA raw sequence reads were aligned to a reference genome (mm10) using STAR version 2.5.2 with default parameters[63]. Gene expression at exons was quantified using HOMER (version 4.11)[64]. DE RNAs were then normalized and identified using DESeq2 (version 1.30.1)[65] with an adjusted FDR < 0.05. Control-specific and consensus DE genes were plotted as Venn diagrams using DiVenn[66]. GO analysis was performed using Metascape[67]. Heat maps were generated with GraphPad Prism versions 9 and 10. Principal component analysis was performed using ClustVis[68].

Nascent RNA-seq

For in vivo nascent RNA-seq, animals were treated with FX-1 (50 mg per kg body weight; Cayman Chemical) or DMSO (solvent control) for 3 h and then injected with 5-ethynyl-uridine 1 h before euthanasia. One half of a harvested quadriceps muscle was processed for total RNA as described above. Then, 5-ethynyl-uridine-labelled nascent RNAs were biotinylated using the Click-iT Nascent RNA Capture Kit (Invitrogen, C10365), isolated with MyOne Streptavidin T1 magnetic Dynabeads (Invitrogen, 65601), and used to produce sequencing libraries with the Ovation SoLo RNA-seq System (Tecan, 0407–32). Libraries were sequenced with 100-bp SE reads on an Illumina NextSeq 2000. Reads were aligned to the mm10 reference genome using STAR version 2.5.2 with default parameters. PCR duplicates were removed using Tecan's Duplicate Marking Tool, NuDup (https://tecangenomics.github.io/nudup/). Expression was quantified with HOMER using the analyzerepeats.pl command with the --count genes option. Differential expression was analysed as described for mRNA sequencing.

Chromatin immunoprecipitation followed by sequencing

For H3K27ac ChIP–seq, a single quadriceps from each animal was processed and nuclei were isolated and sonicated as described previously[16]. Samples were incubated with 5 μg rabbit anti-H3K27ac (Active Motif, 39133) overnight. Antibody complexes were precipitated with anti-rabbit IgG-conjugated paramagnetic beads (Thermo Fisher, 11203D). For BCL6 ChIP–seq, quadriceps from five animals were pooled. Muscles were harvested, minced and processed using a Polytron tissue homogenizer in homogenization buffer (0.15 mM NaCl, 0.05 mM EDTA pH 7.5, 0.5 mM Tris, 0.5% NP40 (Sigma, 18896), 1% Triton X-100). The homogenate was then dounced (~10 strokes) and serially filtered from 150 μm to 30 μm (Sysmex 04–0042-2319, 2317, 2315). Filtrate was spun at 600*g* for 10 min and the isolated nuclei were crosslinked at room temperature with 2 mM disuccinimidyl glutarate (Proteochem, C1104) for 20 min and then with 1% formaldehyde for 5 min. After quenching with 125 mM glycine, crosslinked nuclei were rinsed with PBS and sheared in buffer containing 1% SDS, 10 mM EDTA and 50 mM Tris for six cycles (30 s on, 30 s off) using a Diagenode Bioruptor into 200–1,000-bp fragments. Chromatin was incubated with 5 μg of antibody against BCL6 (ref. 18) overnight, and antibody complexes were precipitated with anti-guinea pig IgG (AbCam, ab6698) conjugated paramagnetic beads (Thermo Fisher, 14203). Immunoprecipitates were washed and decrosslinked. DNA was isolated using MinElute PCR purification kits (QIAGEN, 28006) and used to generate sequencing libraries using KAPA HyperPrep kits (Roche, KK8504). Adaptor-ligated ChIP DNA was size selected to obtain inserts of 200–500 bp using a PippenHT (Sage Science, HTC2010). Libraries were assessed by both a Bioanalyzer High Sensitivity DNA kit

(Agilent, 5067–4627) and qPCR-based quantification (Kapa Biosystems, KK4824) and sequenced using Illumina NextSeq 500 and 2000 instruments.

Analysis of ChIP–seq data

For ChIP–seq, reads were aligned to the mm10 reference genome with Bowtie (version 1.1.2)[69] using --m 1 and --best parameters. Tag directories were generated using makeTagDirectory using the --tbp 1 option. Further analysis was performed with HOMER[64]. Super-enhancers were identified from H3K27ac ChIP–seq data in mouse quadriceps with the findPeaks command, specifying --style super (FDR = 0.001) using Gene Expression Omnibus (GEO) datasets GSM3515055, GSM3515056 and an additionally deposited dataset. The makeUCSCfile command was used to generate H3K27ac ChIP–seq UCSC browser tracks. BCL6 peaks were identified using the findPeaks command, specifying --style factor and --fdr 0.0000001 for stringent peak calling and annotated to nearest genes using annotatePeaks.pl. HOMER's findMotifsGenome. pl command was used to perform motif analysis using --size 200 and --mask with standard background. Gene ontologies near BCL6 ChIP–seq peak were generated using GREAT[70] for regions 5 kb upstream and 1 kb downstream of the TSS plus distal extensions up to 1,000 kb. Cistrome-GO[40] was used to integrate RNA-seq and BCL6 ChIP–seq data and calculate regulatory potential scores. The makeBigWig.pl command was used to generate browser tracks for BCL6, H3K27ac and RNA-seq data. H3K27ac tag density was quantified within a 1-kb vicinity of BCL6 peaks by using HOMER's annotatePeaks.pl command, with --size 1000 option for scatterplots. GraphPad Prism was used to generate box plots of H3K27ac tags in different genotypes. Integrated analysis of Motif Activity and Gene Expression (IMAGE)[55] was used to predict transcription factor activities accounting for changes in gene expression (https://github.com/JesperGrud/IMAGE/).

In vivo protein synthesis and degradation analysis

Rates of muscle protein synthesis were determined by following incorporation of ^{2}H from $^{2}H_2O$ into newly made protein-bound alanine as described previously[46]. Mice were given 0.7 ml intraperitoneal injections of ^{2}H-labelled saline (9 g of NaCl in 1 l of 99.9% $^{2}H_2O$; deuterium oxide; Sigma, 151882). Mice were euthanized at 1 (day 0), 24 (day 1), 48 (day 2), 96 (day 4) and 168 (day 7) hours after the injection, and serum and skeletal muscles were collected. This was followed by sample processing and GC–MS analysis. The deuterium decay curve of body water was used to compute turnover rates. ^{2}H-labeling of protein-bound alanine in muscle was quantified by GC–MS (Agilent Chemstation Mass Spectrometry Software E.02.02.1431), while alanine concentration was determined using the coupled reaction of alanine transaminase and lactate dehydrogenase. Mathematical modelling was performed based on a two-compartment model with free deuterium in body water (precursor) and deuterium incorporated into protein-bound alanine (product) in muscle tissue. Non-linear least-square fitting mathematical algorithms were used to estimate rate constants and synthesis rates were determined.

Puromycin incorporation

For all in vivo measurements of protein synthesis with SUnSET[47], puromycin solution (0.04 μmol per gram body weight in 200 μl of PBS) was injected into mice via intraperitoneal

injection. Muscles were collected after 30 min and processed for western blotting with α-puromycin antibodies.

Autophagic flux

For autophagic flux experiments, mice were given intraperitoneal injections of colchicine (0.4 mg per kg body weight per day) or water for 3 d before muscle collection. Harvested quadriceps muscles were processed for protein and subjected to western blot using anti-LC3A/LC3B (Cell Signaling, 12741). Flux was determined as the difference in normalized LC3-II levels in mice treated with colchicine versus vehicle for each genotype.

Ribosomal sequencing and analysis

To generate ribosome footprints, quadriceps muscles from *Bcl6*$^{i\text{-MKO}}$ and control RiboTag animals were harvested and snap frozen in liquid nitrogen 3 weeks after tamoxifen treatment. Frozen tissue was pulverized, and approximately 50 mg was retained for matched RNA-seq libraries. The remaining material was resuspended in 1 ml per 200 mg Polysome Lysis Buffer (20 mM Tris pH 7.5, 100 mM KCl, 5 mM $MgCl_2$, 1% Tween 20, 0.25% Na-deoxycholate) supplemented with 1× protease inhibitors (Roche) and 100 μg ml^{-1} cycloheximide, rested on ice for 10 min, dounced 10× with a tight pestle, incubated for 10 min on ice, then cleared by centrifugation at 12,000*g* for 10 min at 4 °C. Approximately 3 μl of T1 RNase (Roche, EN0541) was added and incubated at 37 °C for 45 min. After quenching with 15 μl SUPERase−In (Invitrogen, AM2696), 50 μl of magnetic anti-HA beads (Pierce 88836) was added and incubated at room temperature for 1 h with rotation. Beads were washed 3× with high-salt Polysome Wash Buffer (20 mM Tris pH 7.5, 300 mM KCl, 10 mM $MgCl_2$, 1% Tween 20, 0.25% Na-deoxycholate) supplemented with 1× protease inhibitor. Bead-bound RNA was extracted with TRIzol and precipitated overnight with isopropanol and NaOAc at −80 °C. RNA was pelleted and resuspended in a poly-nucleotide kinase reaction (5 μl 2× ligation buffer, 1 μl PNK, 1 μl SUPERase−In, 3 μl H_2O), incubated at 37 °C for 30 min and run out on a 15% polyacrylamide TBE-urea gel. Fragments between 34-nucleotide and 26-nucleotide markers were extracted from the gel in RNA gel extraction buffer (300 mM NaOAc, 1.0 mM EDTA, 0.25% (wt/vol) SDS) overnight. RNA footprints were precipitated overnight with isopropanol and NaOAc at −80 °C, resuspended in 7 μl RNase-free H_2O and used to produce libraries using the NEBNext Small RNA Library Prep Kit. Libraries were sequenced with 50 bp SE reads on an Illumina HiSeq 4000 instrument.

RPFs were processed as follows. Adaptors were trimmed (NEBNext Small RNA read1 adaptor – AGATCGGAAGAGCACACGTCTGAACTCCAGTCAC) and reads filtered for minimum length of 18 nucleotides using Cutadapt[71]. Reads were then aligned against a list of non-coding RNAs using Bowtie. Unaligned RPF reads were next aligned to the mm10 reference genome using STAR[63] with the following options: --outFilterScoreMinOverLread 0.3, --outFilterMatchNminOverLread 0.3. Matched RNA samples were processed with STAR using default settings. Raw RPF and RNA read count matrices were generated with HOMER using the analyzerepeats.pl command with the --noadj option. Metagene plots were generated with HOMER using the makeMetaGeneProfile.pl command with the options --gbin 50, --gRatio 5, --size 500 and --histNorm 10. Changes in TE were detected with

RiboDiff (v0.2.1)[72]. Quality-control metrics for mapping and RPF length were determined using RiboToolKit[73].

MyoAAV infections

MyoAAV4A viruses encoding *Eif4ebp1* shRNAs driven by the U6 promoter were produced by Vector Biolabs. For in vivo knockdown, mice were infected with 1×10^{12} viral copies per mouse via retro-orbital injection. shRNA sequences are listed below.

1. CCGGGTCACAATTTGAGATGGACATCTCGAGATGTCCATCTCAAATTGT GACTTTTTG
2. CCGGAGGCGGTGAAGAGTCACAATTCTCGAGAATTGTGACTCTTCACC GCCTTTTTTG

Data collection and statistical analysis

For animal experiments, aged-matched mice with littermate controls were utilized. For experiments requiring treatments or conditions, mice or cells of a given genotype were randomized to generate experimental groups. Data collection was performed with blinding, but analysis was not performed blind to the conditions of experiments. All animals and data points are shown. We used Microsoft Excel v16 and GraphPad Prism v9 and v10 to perform the statistical analyses. Two-sided Student's unpaired *t*-test with Welch correction or one-way ANOVA with Dunnett's multiple-comparisons tests were used to compare body and tissue weights, muscle functional parameters, qPCR gene expression and protein densitometry between two or multiple groups, respectively. Two-way repeated-measures ANOVA with Tukey's multiple-comparisons test was used to compare the time course of body composition analysis in $Bcl6^{i\text{-MKO}}$ mice. One-way ANOVA with Tukey's correction was performed on normalized ChIP–seq tag counts to compare $Bcl6^{i\text{-MKO}}$ versus Cre^{-} tmx samples. Kolmogorov–Smirnov testing was used to analyse TE. No statistical methods were used to predetermine sample sizes, but our sample sizes were similar to those reported in previous publications characterizing muscle mass and function and gene regulation[4,6,15,28,46,47,51]. Data distribution was assumed to be normal, but this was not formally tested. Sample sizes and *P* values are listed in the figure legends.

Extended Data

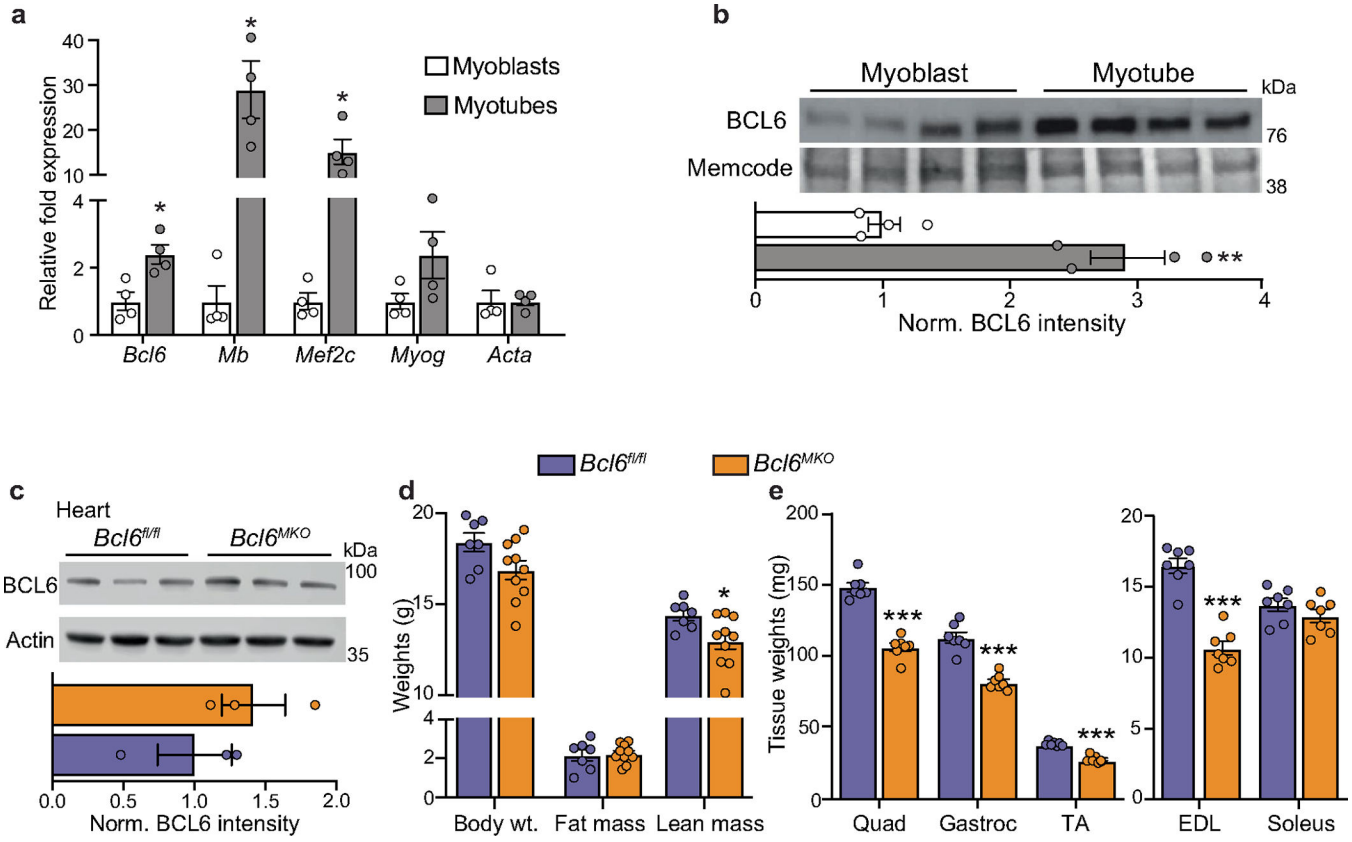

Extended Data Fig. 1 |. *Bcl6* controls the development of skeletal muscle mass.

(**a**) qPCR expression of *Bcl6* and myogenic markers in primary myoblasts and myotubes relative to the housekeeping gene *Rn45s* (n = 4 per group). Myoblast vs myotube *P*-value for *Bcl6* = 0.0124, *Mb* = 0.0153, *Mef2c* = 0.0146 by unpaired, two-tailed t-test with Welch correction. (**b**) Western blot and densitometry of BCL6 and total (Memcode) protein in primary myoblasts and myotubes (n = 4/group). Myoblast vs myotube *P* = 0.0036 by unpaired, two-tailed t-test with Welch correction. (**c**) Western blot and densitometry of BCL6 and Actin protein in heart from $Bcl6^{fl/fl}$ and $Bcl6^{MKO}$ mice (n = 3/group). (**d**) Total body weight, fat, and lean mass in n = 7 $Bcl6^{fl/fl}$ and n = 10 $Bcl6^{MKO}$ female mice at 8 weeks of age. $Bcl6^{fl/fl}$ vs $Bcl6^{MKO}$ lean mass *P* = 0.0184 by unpaired, two-tailed t-test with Welch correction. (**e**) Tissue weights of quadriceps (quad), gastrocnemius (gastroc), tibialis anterior (TA), extensor digitorum longus (EDL) and soleus from female $Bcl6^{fl/fl}$ and $Bcl6^{MKO}$ mice at 16 weeks of age (n = 7/group). Unpaired, two-tailed t-test with Welch correction was performed and all p-values can be found in the source data file. All data are represented as mean ± SEM. * $p < 0.05$, ** $p < 0.01$ and *** $p < 0.001$.

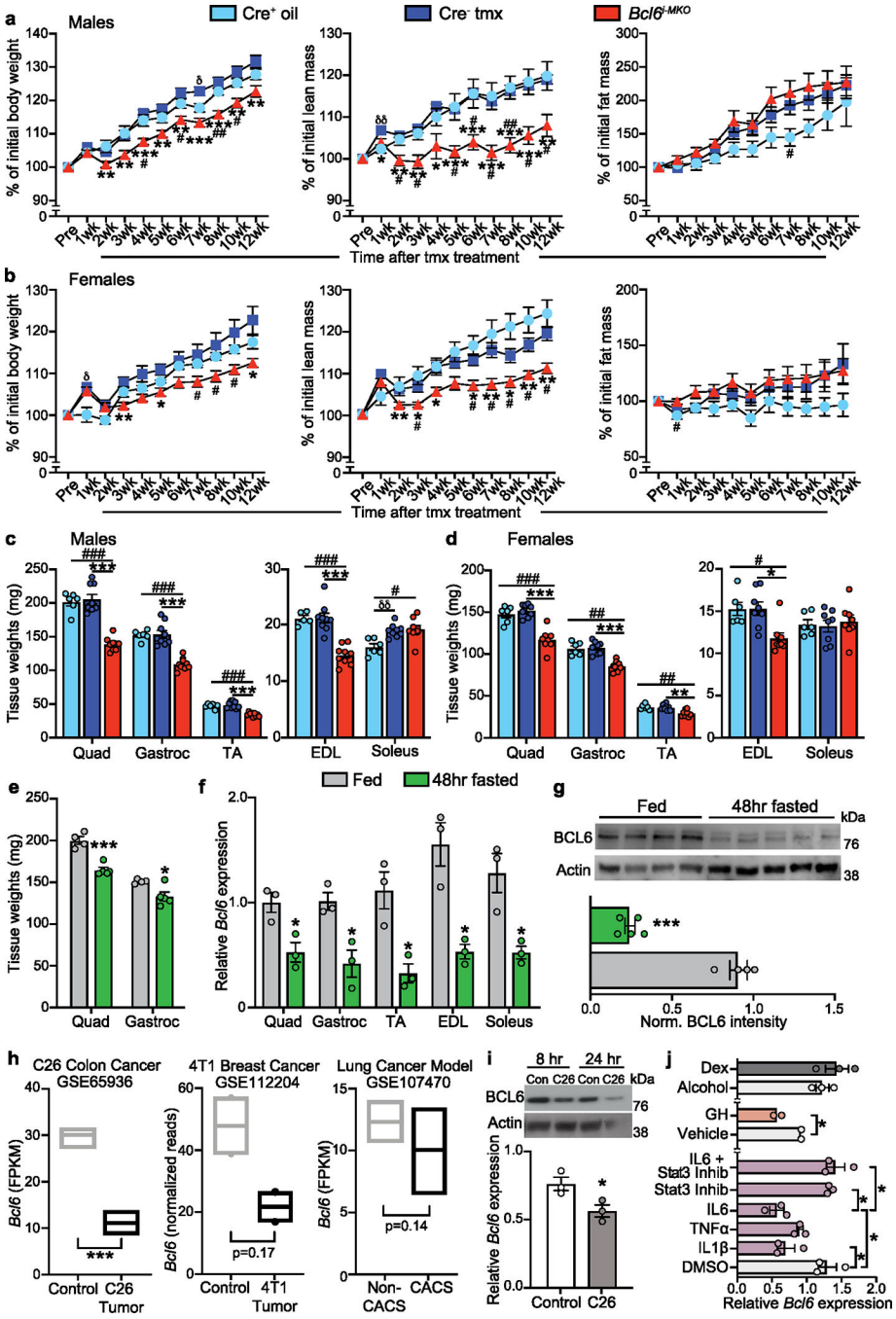

Extended Data Fig. 2 |. Inducible deletion of *Bcl6* in adult mice results in muscle loss.

(**a, b**) Serial measurements of total body, lean, and fat mass in (a) n = 6 Cre^+ oil, n = 9 Cre^-tmx and n = 9 $Bcl6^{i\text{-}MKO}$ male and (b) n = 6 Cre^+oil, n = 8 Cretmx and n = 8 $Bcl6^{i\text{-}MKO}$ female mice starting at 8 weeks of age prior to (pre) and up to 12 weeks after treatment. Two-way ANOVA with Tukey's multiple comparisons test was performed. (**c, d**) Weights of quadriceps (quad), gastrocnemius (gastroc), tibialis anterior (TA), extensor digitorum longus (EDL) and soleus from Cre^+ oil, Cre^-tmx and $Bcl6^{i\text{-}MKO}$ (c) male and (d) female mice 12 weeks after treatment (n = same as (a,b)). One-way ANOVA with Dunnett's

multiple comparisons test was performed. (**e**) Tissue weights in n = 4 *ad lib* chow fed and n = 5 48-hour fasted C57BL/6 male mice. (**f**) qPCR of *Bcl6* normalized to *36b4* in muscles from fed and 48-hour fasted mice (n = 3/group). (**g**) Western blot and densitometry of BCL6 and Actin in n = 4 fed and n = 5 from 48 hour fasted mouse quadriceps. Unpaired, two-tailed t-test with Welch correction was performed in (e-g). (**h**) *Bcl6* levels in published cancer-associated cachexia syndrome (CACS) models. GEO accession numbers are listed. Control vs C26 colon cancer $P = 0.0008$ by unpaired, two-tailed t-test with Welch correction (n = 3/group). Boxplot shows min to max values with line at the mean. (**i**) *Bcl6* expression in C2C12 myotubes exposed to 33% colon-26 carcinoma (C26) conditioned versus control media for 8 hours (n = 3/group; unpaired, two-tailed t-test with Welch correction was performed) and corresponding protein blots after 8 or 24 hours. (**j**) *Bcl6* expression in C2C12 myotubes treated with cytokines (n = 3/group), growth hormone (n = 2/group) and glucocorticoids (n = 3/group) for 8 hours. Unpaired, two-tailed t-test with Welch correction and one-way ANOVA with Dunnett's multiple comparisons were performed. Exact p-values can be found in the source data file. All data in (a-g) and (i-j) are represented as mean ± SEM. δ $p < 0.05$, δδ $p < 0.01$ for Cre^+ oil vs Cre^-tmx; # $p < 0.05$, ## $p < 0.01$, ### $p < 0.001$ for Cre^+ oil vs $Bcl6^{i\text{-}MKO}$; * $p < 0.05$, ** $p < 0.01$, *** $p < 0.001$ for Cre^-tmx vs $Bcl6^{i\text{-}MKO}$ or fed vs fasted or vehicle vs treated myotubes.

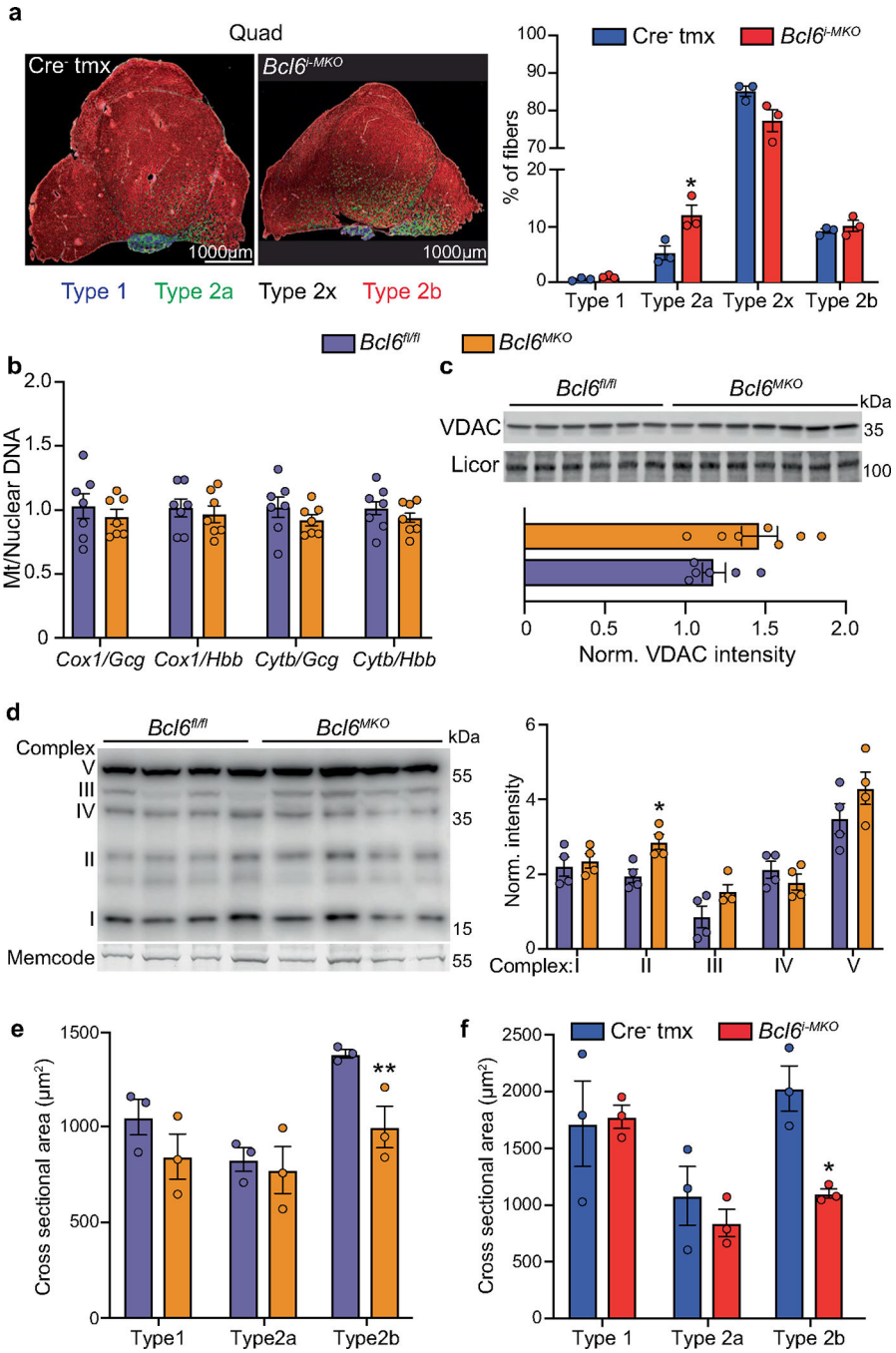

Extended Data Fig. 3 |. *Bcl6* controls an oxidative to glycolytic shift in myofibres.

(**a**) Representative fluorescent antibody-stained images of four myosin heavy chain isoforms in quadriceps from Cre⁻ tmx and *Bcl6*$^{i\text{-}MKO}$ mice (left). MYH7 (type 1 fiber) is blue, MYH2 (type 2a fiber) is green, MYH1 (type 2x fiber) is black, and MYH4 (type 2b fiber) is red. Quantification of fiber types (right) expressed as percentage of total (n = 3/group). Cre⁻ tmx vs *Bcl6*$^{i\text{-}MKO}$ type 2a fiber $P = 0.0374$ by unpaired, two-tailed t-test with Welch correction. (**b**) qPCR DNA ratios of mitochondrial genes *Cox1* and *Cytb* over nuclear genes *Gcg* and *Hbb* in quadriceps from *Bcl6*$^{fl/fl}$ and *Bcl6*^{MKO} males (n = 7/group). (**c**) Western

blot and densitometry of VDAC and total (Licor) protein in quadriceps from n = 6 *Bcl6*$^{fl/fl}$ and n = 7 *Bcl6*^{MKO} males. (**d**) Protein levels of mitochondrial complex subunits and total (Memcode) protein in quadriceps from *Bcl6*$^{fl/fl}$ and *Bcl6*^{MKO} mice. Western blot (left) and protein densitometry (right) are shown. (n = 4/group) *Bcl6*$^{fl/fl}$ vs *Bcl6*^{MKO} complex II P = 0.0139 by unpaired, two-tailed t-test with Welch correction. (e, f) Cross-sectional areas of specific fiber types determined from fluorescent antibody-stained sections in quadriceps from (**e**) *Bcl6*$^{fl/fl}$ and *Bcl6*^{MKO} mice (n = 3/group) and (**f**) Cre^{-} tmx and *Bcl6*$^{i\text{-}MKO}$ mice (n = 3/group). Type 2b fiber in *Bcl6*$^{fl/fl}$ vs *Bcl6*^{MKO} P = 0.003 and in Cre^{-} tmx vs *Bcl6*$^{i\text{-}MKO}$ P = 0.0385 by unpaired, two-tailed t-test with Welch correction. All data are represented as mean ± SEM. * p < 0.05, ** p < 0.01.

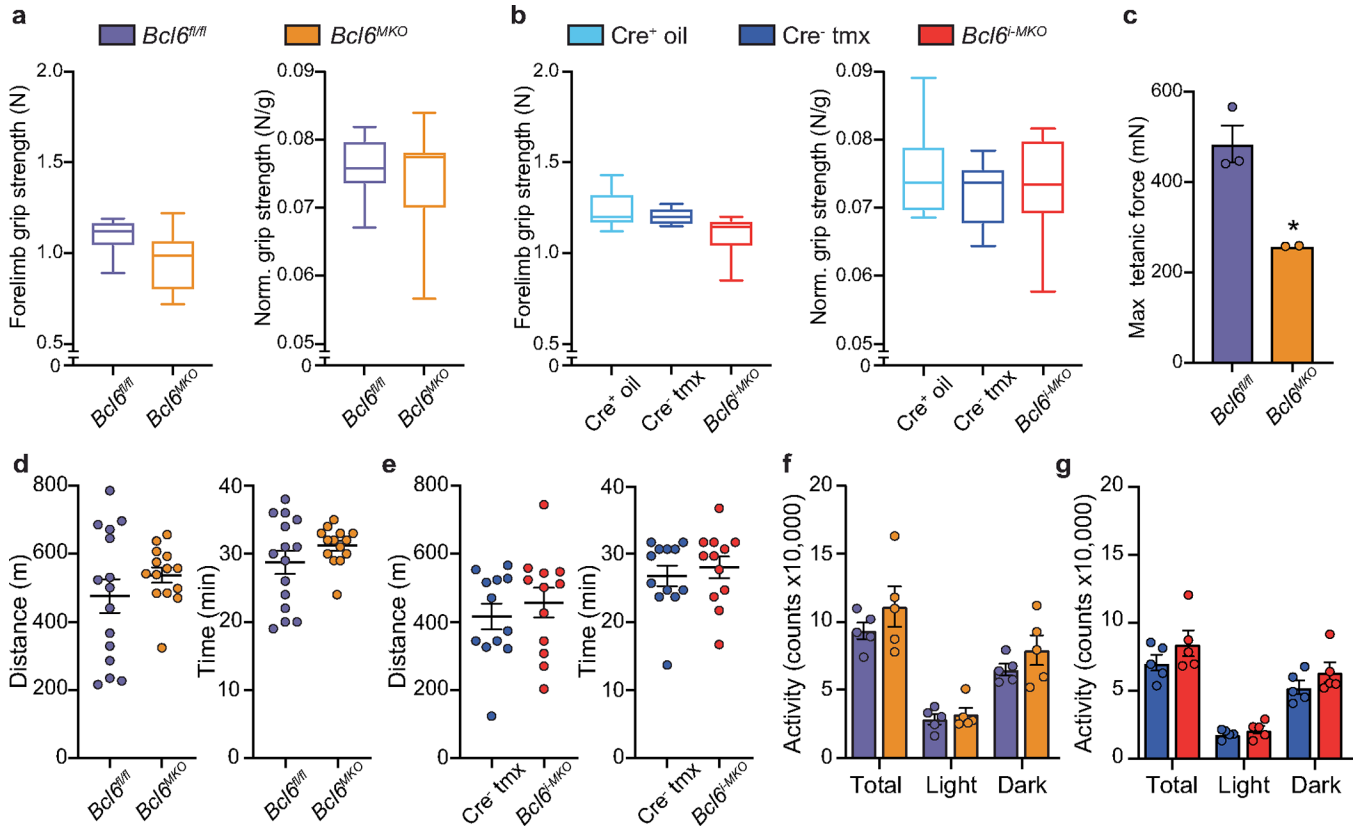

Extended Data Fig. 4 |. Muscle loss due to *Bcl6* deletion is associated with reduced muscle function.

(**a, b**) Absolute (left) and lean body mass normalized (right) forelimb grip strength measured in (a) 13-week old n = 7 *Bcl6*$^{fl/fl}$ and n = 10 *Bcl6*^{MKO} female mice and (b) n = 6 Cre^{+} oil, n = 8 Cre^{-} tmx and n = 8 *Bcl6*$^{i\text{-}MKO}$ female mice twelve weeks after tamoxifen or oil treatment. Whiskers in the boxplot show min to max values with line at the median and box representing the first to third quartile values. (**c**) Maximum tetanic force for the tibialis anterior (TA) muscle from 13-week old n = 3 *Bcl6*$^{fl/fl}$ and n = 2 *Bcl6*^{MKO} female mice (P-value for maximum force = 0.0311 by unpaired, two-tailed t-test with Welch correction). (**d, e**) Distance and time run on a treadmill to exhaustion in (d) 13-week old n = 15 *Bcl6*$^{fl/fl}$ and n = 14 *Bcl6*^{MKO} male mice and (e) Cre^{-} tmx and *Bcl6*$^{i\text{-}MKO}$ female mice twelve weeks after tamoxifen treatment (n = 12/group). (**f, g**) Light phase, dark phase and total activity

in (f) 13-week old *Bcl6*$^{fl/fl}$ and *Bcl6*^{MKO} male mice (n = 5/group) and (g) Cre^{-} tmx and *Bcl6*$^{i\text{-}MKO}$ male mice 1.5 weeks after tamoxifen treatment (n = 5/group). All data in (c-g) are represented as mean ± SEM. * p< 0.05.

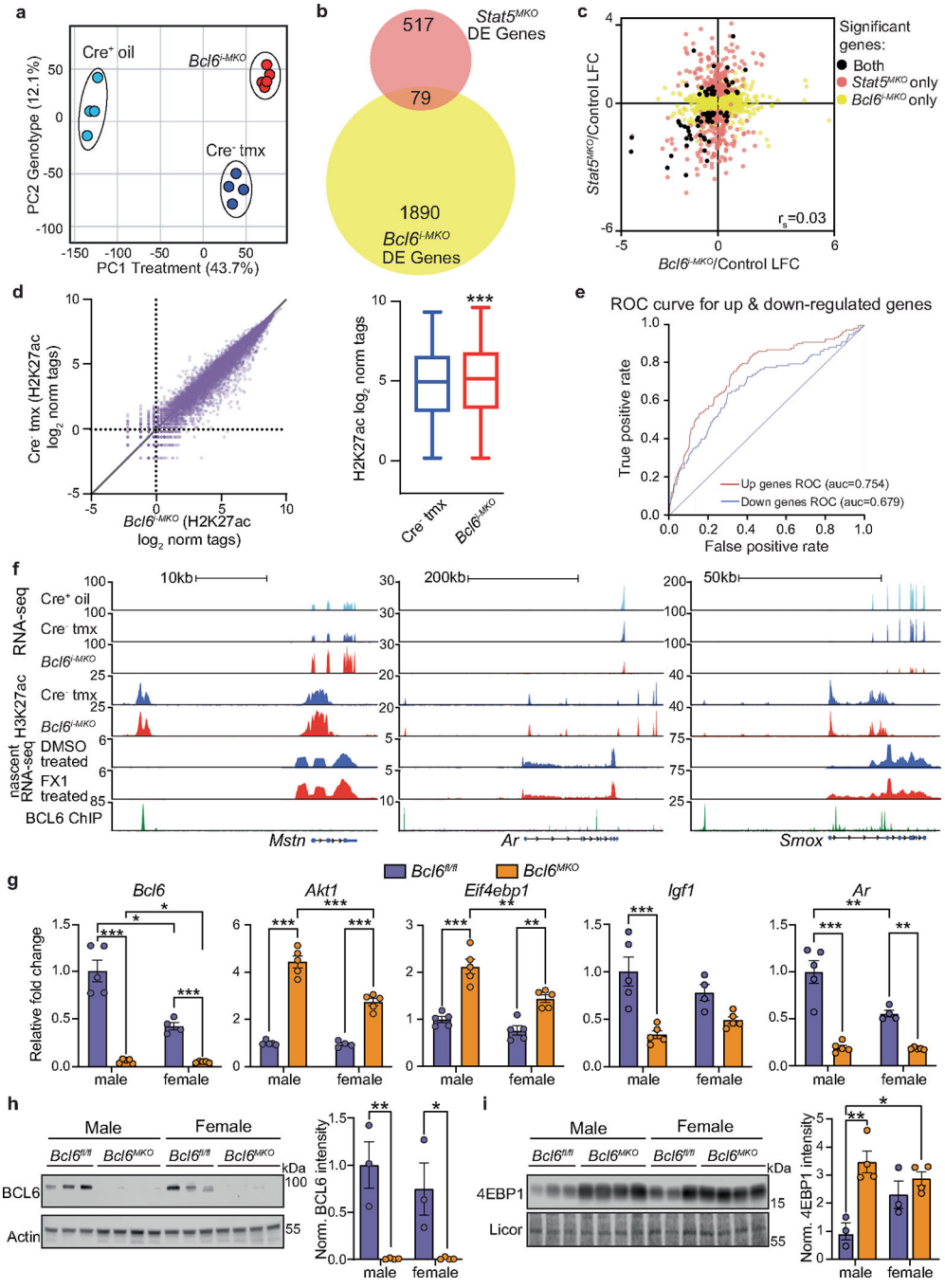

Extended Data Fig. 5 |. BCL6 directly controls the expression of anabolic regulators.

(**a**) Principal component analysis of RNA-seq from n = 5 *Bcl6*$^{i\text{-}MKO}$ and n = 4 tamoxifen-treated controls (Cre^{-} tmx) or n = 4 corn oil-treated controls (Cre^{+} oil). (**b**) Venn diagram depicting overlap between differentially expressed (DE) genes in muscle *Stat5*

knockout (*Stat5*^{MKO}) mice (GEO series GSE14710) compared to muscle *Bcl6*$^{i\text{-}MKO}$ mice. (**c**) Quadrant plot of $\log_2$ fold change in gene expression in *Stat5*^{MKO}/controls versus *Bcl6*$^{i\text{-}MKO}$/Cre^{-} tmx controls. Spearman correlation coefficient $r_s = 0.03$. (**d**) Scatterplot (left) of normalized H3K27ac tag counts and boxplot (right) showing quantification of H3K27ac tag densities within 1kb of BCL6 peaks in Cre^{-} tmx and *Bcl6*$^{i\text{-}MKO}$ quadriceps (n = 3/group; $P = 3.5e^{-10}$ by unpaired, two-tailed Mann Whitney test). Whiskers in the boxplot show min to max values with line at the median and box representing the first to third quartile values. (**e**) Receiver operator curve (ROC) of the association between differential expression in *Bcl6*-ablated muscle and BCL6 binding peaks. (**f**) UCSC browser tracks of RNAseq in quadriceps from Cre^{+} oil, Cre^{-} tmx and *Bcl6*$^{i\text{-}MKO}$ mice, H3K27ac ChIP-seq in quadriceps from Cre^{-} tmx and *Bcl6*$^{i\text{-}MKO}$ mice 1 week after oil or tamoxifen treatment, nascent RNA-seq in quadriceps from mice treated with DMSO or FX1 for 3 hours, and BCL6 ChIP-seq track in quadriceps from C57BL/6 animals along the *Mstn*, *Ar*, and *Smox* genes. (**g**) qPCR expression of *Bcl6, Akt1, Eif4ebp1, Igf1* and *Ar* in quadriceps from males (n = 5/group) and females (n = 4 *Bcl6*$^{fl/fl}$ and n = 5 *Bcl6*^{MKO} mice). Two-way ANOVA followed by Tukey's multiple comparisons test was performed and all individual p-values can be found in the source data file. (**h, i**) Western blot and densitometry of (h) BCL6 and actin (i) 4EBP1 and total protein (licor) in quadriceps from male and female n = 3 *Bcl6*$^{fl/fl}$ and n = 4 *Bcl6*^{MKO} mice. For BCL6, *P*(male *Bcl6*$^{fl/fl}$ vs *Bcl6*^{MKO}) = 0.005, *P*(male *Bcl6*$^{fl/fl}$ vs female *Bcl6*^{MKO}) = 0.005, *P*(male *Bcl6*^{MKO} vs female *Bcl6*$^{fl/fl}$) = 0.0299, *P*(female *Bcl6*$^{fl/fl}$ vs *Bcl6*^{MKO}) = 0.0305 and for 4EBP1, *P*(male *Bcl6*$^{fl/fl}$ vs *Bcl6*^{MKO}) = 0.0034, *P*(male *Bcl6*$^{fl/fl}$ vs female *Bcl6*^{MKO}) = 0.0199 by two-way ANOVA followed by Tukey's multiple comparisons. All data in (g-i) are represented as mean ± SEM. * $p < 0.05$, ** $p < 0.01$ and *** $p < 0.001$.

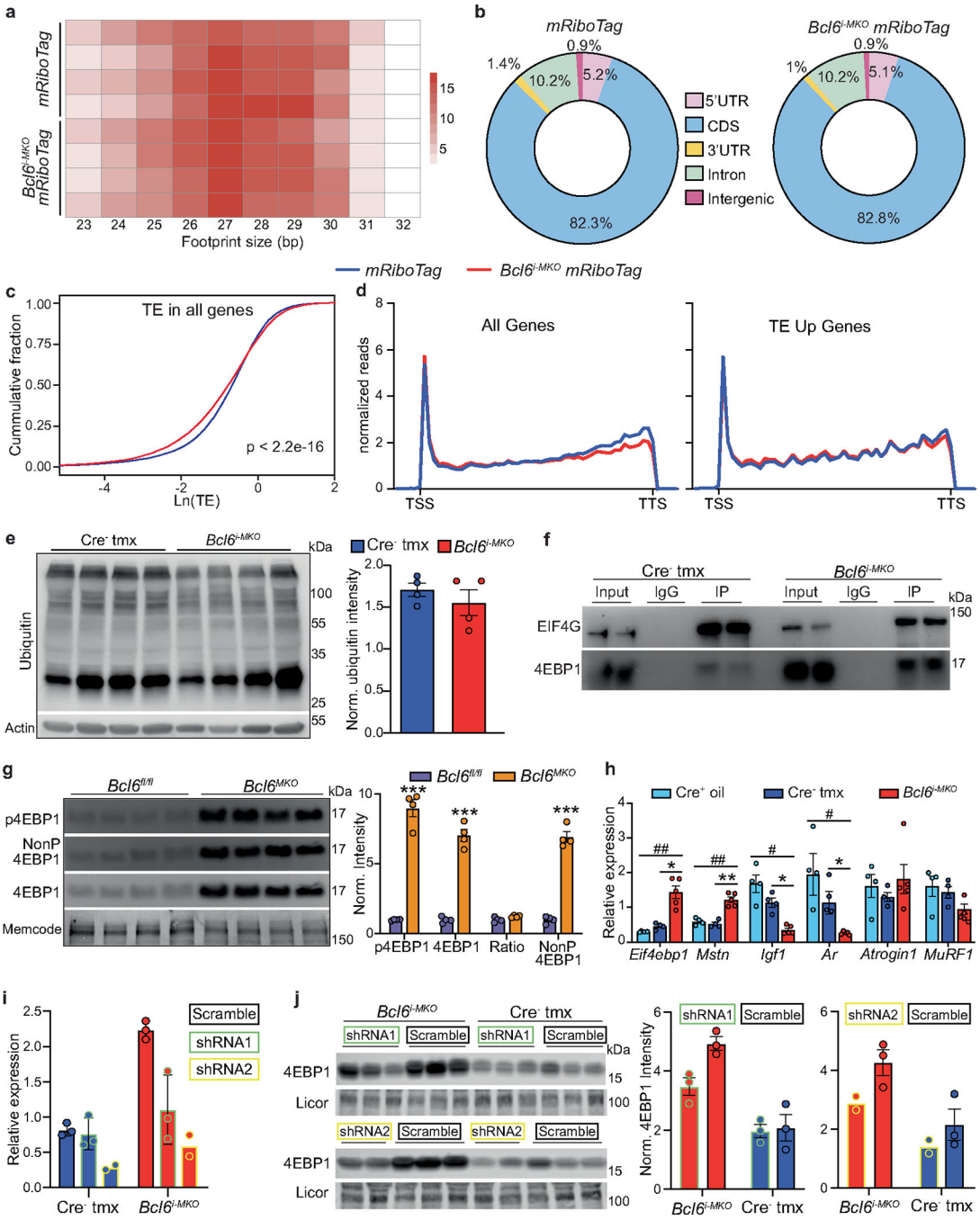

Extended Data Fig. 6 |. Loss of *Bcl6* reduces the rate of muscle protein synthesis.

(**a**) Heatmap of ribosome protected fragment (RPF) sizes in sequencing libraries of tamoxifen-treated *Bcl6*$^{i\text{-}MKO}$*mRiboTag* and *mRiboTag* mice. (**b**) Pie chart distribution of mapped RPF reads. (**c**) Empirical cumulative distribution frequency (Ecdf) plots of the translation efficiencies (natural logarithm of TE) in quadriceps for all genes. *Bcl6*$^{i\text{-}MKO}$ *mRiboTag* vs *mRiboTag* $P = 2.2e\text{-}16$ by two-sided Kolmogorov-Smirnov testing (**d**) Metagene distribution plot showing normalized ribo-seq RPF reads from the TSS to TTS for all genes (left) and genes with increased TE (right). (**e**) Western blot and densitometry

of ubiquitin protein and actin in quadriceps from Cre^{-} tmx and *Bcl6*$^{i\text{-}MKO}$ males 1.5 weeks after tamoxifen treatment (n = 4/group). (**f**) EIF4E co-immunoprecipitation and western blots for EIF4G (top) and 4EBP1 (bottom) in gastrocnemius from Cre^{-} tmx and *Bcl6*$^{i\text{-}MKO}$ males 1 week after tamoxifen treatment (n = 2/group). (**g**) Western blot and densitometry of p4EBP1, Non-phospho 4EBP1, Total 4EBP1, and total (Memcode) protein in quadriceps from 10 week old *Bcl6*$^{fl/fl}$ and *Bcl6*^{MKO} males (n = 4/group). *P*(*Bcl6*$^{fl/fl}$ vs *Bcl6*^{MKO}) for p4EBP1 = 0.0009, total 4EBP1 = 0.0004, and nonP 4EBP1 = 0.0002 by unpaired, two-tailed t-test with Welch correction. (**h**) qPCR of protein synthesis and degradation regulators in n = 4 Cre^{+} oil, n = 4 Cre^{-} tmx and n = 5 *Bcl6*$^{i\text{-}MKO}$ male mice 7 days after treatment. One-way ANOVA with Dunnett's multiple comparisons test showed that *P*(Cre^{+} oil vs *Bcl6*$^{i\text{-}MKO}$) for *Eif4ebp1* = 0.0086, *Mstn* = 0.0018, *Igf1* = 0.0332 and *Ar* = 0.0420; *P*(Cre^{-} tmx vs *Bcl6*$^{i\text{-}MKO}$) for *Eif4ebp1* = 0.0163, *Mstn* = 0.0011, *Igf1* = 0.0140 and *Ar* = 0.0330. **(i, j**) Analysis of *Eif4ebp1* knockdown efficiency in muscles (n = 3 mice/group for scramble and *Eif4ebp1* shRNA1 and n = 2 mice/group for *Eif4ebp1* shRNA2). (i) qPCR of *Eif4ebp1* and (j) western blot and densitometry of 4EBP1 in Cre^{-} tmx and *Bcl6*$^{i\text{-}MKO}$ male mice transduced with scramble (black border), *Eif4ebp1* shRNA1 (green border), or *Eif4ebp1* shRNA2 (yellow border) and treated with tamoxifen one week after viral infection. Tissues were analyzed eight weeks later. All bar graph data in (e, g-j) are represented as mean ± SEM. # $p < 0.05$, ## $p < 0.01$ for Cre^{+} oil vs *Bcl6*$^{i\text{-}MKO}$ and * $p < 0.05$, ** $p < 0.01$, *** $p < 0.001$ for Cre^{-}tmx vs *Bcl6*$^{i\text{-}MKO}$ and *Bcl6*$^{fl/fl}$ vs *Bcl6*^{MKO}.

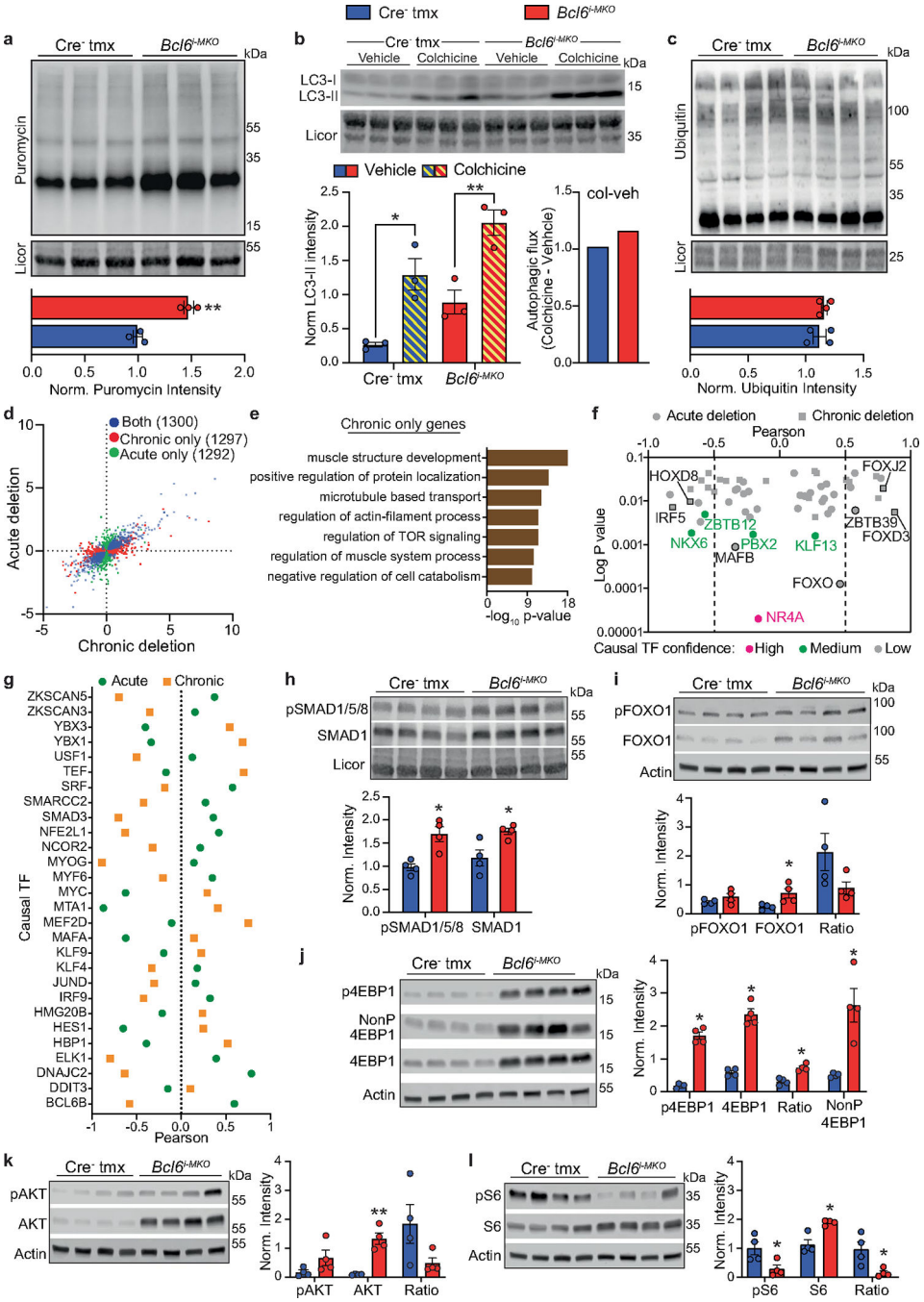

Extended Data Fig. 7 |. Chronic *Bcl6* loss evokes compensatory signaling to maintain muscle mass.

(**a**) SUnSET analysis of puromycin incorporation into quadriceps (top) in Cre^{-} tmx and *Bcl6*$^{i\text{-}MKO}$ mice 12 weeks after tamoxifen treatment. Puromycin labeling relative to total protein (Licor) by densitometry (bottom) (n = 3/group; $P = 0.0017$ by unpaired, two-tailed t-test with Welch correction). (**b**) Western blot and densitometry in quadriceps from Cre^{-} tmx and *Bcl6*$^{i\text{-}MKO}$ males 15 weeks after tamoxifen treatment for LC3, 3 days after colchicine or vehicle treatment. (n = 3/group; Two-way ANOVA followed by Tukey's multiple

comparisons test was performed. *P* (Veh-Cre$^-$ tmx vs Col-Cre$^-$ tmx) = 0.0174; *P* (Veh-Cre$^-$ tmx vs Col-*Bcl6*$^{i\text{-}MKO}$) = 0.0005; *P* (Veh-*Bcl6*$^{i\text{-}MKO}$ vs Col-*Bcl6*$^{i\text{-}MKO}$) = 0.0083.) Flux is the difference in average LC3-II levels in colchicine minus vehicle (bottom right). (**c**) Western blot and densitometry of ubiquitin and total (Licor) protein in quadriceps from Cre$^-$ tmx and *Bcl6*$^{i\text{-}MKO}$ males 12 weeks after tamoxifen treatment (n = 4/group). (**d**) Quadrant plot of log2 fold change in gene expression in *Bcl6*$^{i\text{-}MKO}$/Cre$^-$ tmx 12 weeks after tamoxifen treatment (chronic) versus *Bcl6*^{iMKO}/Cre$^-$ tmx 1 week after tamoxifen treatment (acute). (**e**) Ontology analysis of differential genes unique in chronic *Bcl6* deletion. Cumulative hypergeometric statistical testing was used. (**f**) Log p-value versus Pearson correlation plotted for causal transcription factors identified by IMAGE that were unique to either acute or chronic *Bcl6* deletion. Pink = high, green = medium, and gray = low confidence factors. Factors in acute dataset are shown as circles and factors in chronic are squares. (**g**) Causal transcription factors with opposing Pearson correlations to gene expression in acute versus chronic *Bcl6* deletion. Acute = green circle, chronic = orange square. (**h-l**) Western blot and densitometry of (h) pSMAD1/5/8, Total SMAD1, and total (Licor) protein, (i) pFOXO1, Total FOXO1, and Actin, (**j**) p4EBP1, Non-phospho 4EBP1, Total 4EBP1, and Actin, (**k**) pAKT, Total AKT, and Actin and (**l**) pS6, Total S6, and Actin in quadriceps from Cre$^-$ tmx and *Bcl6*$^{i\text{-}MKO}$ males 12 week after tamoxifen treatment (n = 4/group). Unpaired, two-tailed t-test with Welch correction and all individual p-values can be found in the source data file. All bar graph data in (a-c, h-l) are represented as mean ± SEM. * $p < 0.05$ and ** $p < 0.01$.

Supplementary Material

Refer to Web version on PubMed Central for supplementary material.

Acknowledgements

We thank N. Hay (University of Illinois Chicago), L. Goodyear (Joslin Diabetes Center, Harvard), C. He (Northwestern University), J. Bass (Northwestern University), D. Chakravarti (Northwestern University) and J. Madsen (University of Southern Denmark) for helpful advice and discussion. We thank Northwestern University's NU-Seq Core, Comprehensive Metabolic Core and Mouse Histology and Phenotyping Laboratory (supported by NCI P30-CA060553 awarded to the Robert H Lurie Comprehensive Cancer Center) for services. This research was supported by computational resources provided by the Quest high-performance computing facility at Northwestern University. Figures 1d, 2a, 6c and 8 were created with BioRender.com. This work was funded by Merit Review Award #I01BX004898 from the United States (U.S.) Department of Veterans Affairs (to G.D.B.), National Institutes of Health (NIH) grants R01DK108987 (to G.D.B.) and T32 GM008061 (to E.F.) and Pfizer Aspire award WI183795 (to G.D.B.). M.Q. is supported by NIH grants R56HL158531, R01HL166356–01, R03DK130908–01A1 and R01AG078174–01 and CCHMC grants RIP, CCRF Endowed Scholarship and HI Translational Funds. D.A. is supported by the Searle Scholar Program (grant no. SSP-2023–102). E.M.M. is supported by NIH grants R01HL061322 and R01NS047726. The article contents do not represent the views of the U.S. Department of Veterans Affairs or the United States Government.

Data availability

All sequencing data generated in this study are publicly available in the GEO repository SuperSeries GSE190956. We also utilized publicly accessible RNA-seq and microarray data from GEO repository entries GSE65936, GSE112204, GSE107470 and GSE14710, as well as the mm10 reference assembly for the mouse genome. Source data are provided with this paper.

References

1. Sartori R, Romanello V & Sandri M Mechanisms of muscle atrophy and hypertrophy: implications in health and disease. Nat. Commun. 12, 330 (2021). [PubMed: 33436614]
2. Cohen S, Nathan JA & Goldberg AL Muscle wasting in disease: molecular mechanisms and promising therapies. Nat. Rev. Drug Discov. 14, 58–74 (2015). [PubMed: 25549588]
3. Saxton RA & Sabatini DM mTOR signaling in growth, metabolism, and disease. Cell 169, 361–371 (2017).
4. Bodine SC et al. Identification of ubiquitin ligases required for skeletal muscle atrophy. Science 294, 1704–1708 (2001). [PubMed: 11679633]
5. Brunet A et al. Akt promotes cell survival by phosphorylating and inhibiting a Forkhead transcription factor. Cell 96, 857–868 (1999). [PubMed: 10102273]
6. McPherron AC, Lawler AM & Lee SJ Regulation of skeletal muscle mass in mice by a new TGF-beta superfamily member. Nature 387, 83–90 (1997). [PubMed: 9139826]
7. Goodman CA & Hornberger TA New roles for Smad signaling and phosphatidic acid in the regulation of skeletal muscle mass. F1000Prime Rep. 6, 20 (2014). [PubMed: 24765525]
8. Rossetti ML, Steiner JL & Gordon BS Androgen-mediated regulation of skeletal muscle protein balance. Mol. Cell. Endocrinol. 447, 35–44 (2017). [PubMed: 28237723]
9. Ye BH et al. Alterations of a zinc finger-encoding gene, BCL-6, in diffuse large-cell lymphoma. Science 262, 747–750 (1993). [PubMed: 8235596]
10. Kerckaert JP et al. *LAZ3*, a novel zinc-finger encoding gene, is disrupted by recurring chromosome 3q27 translocations in human lymphomas. Nat. Genet. 5, 66–70 (1993). [PubMed: 8220427]
11. Dent AL, Shaffer AL, Yu X, Allman D & Staudt LM Control of inflammation, cytokine expression, and germinal center formation by BCL-6. Science 276, 589–592 (1997). [PubMed: 9110977]
12. Albagli-Curiel O et al. Increased expression of the LAZ3 (BCL6) proto-oncogene accompanies murine skeletal myogenesis. Differentiation 64, 33–44 (1998). [PubMed: 9921651]
13. Parikh H et al. Molecular correlates for maximal oxygen uptake and type 1 fibers. Am. J. Physiol. Endocrinol. Metab 294, E1152–E1159 (2008). [PubMed: 18445752]
14. Haberland M, Montgomery RL & Olson EN The many roles of histone deacetylases in development and physiology: implications for disease and therapy. Nat. Rev. Genet. 10, 32–42 (2009). [PubMed: 19065135]
15. Yamamoto H et al. NCoR1 is a conserved physiological modulator of muscle mass and oxidative function. Cell 147, 827–839 (2011). [PubMed: 22078881]
16. Ramachandran K et al. Dynamic enhancers control skeletal muscle identity and reprogramming. PLoS Biol. 17, e3000467 (2019). [PubMed: 31589602]
17. Hnisz D et al. Super-enhancers in the control of cell identity and disease. Cell 155, 934–947 (2013). [PubMed: 24119843]
18. Senagolage MD et al. Loss of transcriptional repression by BCL6 confers insulin sensitivity in the setting of obesity. Cell Rep. 25, 3283–3298 (2018). [PubMed: 30566857]
19. Miniou P et al. Gene targeting restricted to mouse striated muscle lineage. Nucleic Acids Res. 27, e27 (1999). [PubMed: 10481039]
20. McCarthy JJ, Srikuea R, Kirby TJ, Peterson CA & Esser KA Inducible Cre transgenic mouse strain for skeletal muscle-specific gene targeting. Skelet. Muscle 2, 8 (2012). [PubMed: 22564549]
21. Wang G et al. Metastatic cancers promote cachexia through ZIP14 upregulation in skeletal muscle. Nat. Med. 24, 770–781 (2018). [PubMed: 29875463]
22. Goncalves MD et al. Fenofibrate prevents skeletal muscle loss in mice with lung cancer. Proc. Natl Acad. Sci. USA 115, E743–E752 (2018). [PubMed: 29311302]
23. Tseng YC et al. Preclinical investigation of the novel histone deacetylase inhibitor AR-42 in the treatment of cancer-induced cachexia. J. Natl Cancer Inst. 107, djv274 (2015). [PubMed: 26464423]
24. Wang Y & Pessin JE Mechanisms for fiber-type specificity of skeletal muscle atrophy. Curr. Opin. Clin. Nutr. Metab. Care 16, 243–250 (2013). [PubMed: 23493017]

25. Ciciliot S, Rossi AC, Dyar KA, Blaauw B & Schiaffino S Muscle type and fiber type specificity in muscle wasting. Int. J. Biochem. Cell Biol. 45, 2191–2199 (2013). [PubMed: 23702032]
26. Zhang Y, Laz EV & Waxman DJ Dynamic, sex-differential STAT5 and BCL6 binding to sex-biased, growth hormone-regulated genes in adult mouse liver. Mol. Cell. Biol. 32, 880–896 (2012). [PubMed: 22158971]
27. Lin G, LaPensee CR, Qin ZS & Schwartz J Reciprocal occupancy of BCL6 and STAT5 on growth hormone target genes: contrasting transcriptional outcomes and promoter-specific roles of p300 and HDAC3. Mol. Cell. Endocrinol. 395, 19–31 (2014). [PubMed: 25088465]
28. Klover P, Chen W, Zhu BM & Hennighausen L Skeletal muscle growth and fiber composition in mice are regulated through the transcription factors STAT5a/b: linking growth hormone to the androgen receptor. FASEB J. 23, 3140–3148 (2009). [PubMed: 19417088]
29. Brooks SA & Blackshear PJ Tristetraprolin (TTP): interactions with mRNA and proteins, and current thoughts on mechanisms of action. Biochim. Biophys. Acta 1829, 666–679 (2013). [PubMed: 23428348]
30. White MR & Garcin ED The sweet side of RNA regulation: glyceraldehyde-3-phosphate dehydrogenase as a noncanonical RNA-binding protein. Wiley Interdiscip. Rev. RNA 7, 53–70 (2016). [PubMed: 26564736]
31. Kejiou NS et al. Pyruvate Kinase M (PKM) binds ribosomes in a poly-ADP ribosylation dependent manner to induce translational stalling. Nucleic Acids Res. 51, 6461–6478 (2023). [PubMed: 37224531]
32. Richter JD CPEB: a life in translation. Trends Biochem. Sci. 32, 279–285 (2007). [PubMed: 17481902]
33. Yang C & Carrier F The UV-inducible RNA-binding protein A18 (A18 hnRNP) plays a protective role in the genotoxic stress response. J. Biol. Chem. 276, 47277–47284 (2001). [PubMed: 11574538]
34. Kawagishi H et al. Hzf regulates adipogenesis through translational control of C/EBPalpha. EMBO J. 27, 1481–1490 (2008). [PubMed: 18418387]
35. Mandal S, Mandal A, Johansson HE, Orjalo AV & Park MH Depletion of cellular polyamines, spermidine and spermine, causes a total arrest in translation and growth in mammalian cells. Proc. Natl Acad. Sci. USA 110, 2169–2174 (2013). [PubMed: 23345430]
36. Dever TE & Ivanov IP Roles of polyamines in translation. J. Biol. Chem. 293, 18719–18729 (2018). [PubMed: 30323064]
37. Hatzi K et al. A hybrid mechanism of action for BCL6 in B cells defined by formation of functionally distinct complexes at enhancers and promoters. Cell Rep. 4, 578–588 (2013). [PubMed: 23911289]
38. Sommars MA et al. Dynamic repression by BCL6 controls the genome-wide liver response to fasting and steatosis. Elife 8, e43922 (2019). [PubMed: 30983568]
39. Barish GD et al. Bcl-6 and NF-kappaB cistromes mediate opposing regulation of the innate immune response. Genes Dev. 24, 2760–2765 (2010). [PubMed: 21106671]
40. Li S et al. Cistrome-GO: a web server for functional enrichment analysis of transcription factor ChIP–seq peaks. Nucleic Acids Res. 47, W206–W211 (2019). [PubMed: 31053864]
41. Cardenas MG et al. Rationally designed BCL6 inhibitors target activated B cell diffuse large B cell lymphoma. J. Clin. Invest. 126, 3351–3362 (2016). [PubMed: 27482887]
42. Langer HT et al. Muscle atrophy due to nerve damage is accompanied by elevated myofibrillar protein synthesis rates. Front. Physiol. 9, 1220 (2018). [PubMed: 30233398]
43. Emery PW, Edwards RH, Rennie MJ, Souhami RL & Halliday D Protein synthesis in muscle measured in vivo in cachectic patients with cancer. BMJ 289, 584–586 (1984). [PubMed: 6087973]
44. Rennie MJ et al. Muscle protein synthesis measured by stable isotope techniques in man: the effects of feeding and fasting. Clin. Sci. 63, 519–523 (1982).
45. Bederman IR, Dufner DA, Alexander JC & Previs SF Novel application of the ‘doubly labeled’ water method: measuring CO2 production and the tissue-specific dynamics of lipid and protein in vivo. Am. J. Physiol. Endocrinol. Metab 290, E1048–E1056 (2006). [PubMed: 16368786]

46. Bederman IR et al. Chronic hindlimb suspension unloading markedly decreases turnover rates of skeletal and cardiac muscle proteins and adipose tissue triglycerides. J. Appl. Physiol. 119, 16–26 (2015). [PubMed: 25930021]
47. Goodman CA et al. Novel insights into the regulation of skeletal muscle protein synthesis as revealed by a new nonradioactive in vivo technique. FASEB J. 25, 1028–1039 (2011). [PubMed: 21148113]
48. Ingolia NT, Ghaemmaghami S, Newman JR & Weissman JS Genome-wide analysis in vivo of translation with nucleotide resolution using ribosome profiling. Science 324, 218–223 (2009). [PubMed: 19213877]
49. Ju JS, Varadhachary AS, Miller SE & Weihl CC Quantitation of 'autophagic flux' in mature skeletal muscle. Autophagy 6, 929–935 (2010). [PubMed: 20657169]
50. Barth S, Glick D & Macleod KF Autophagy: assays and artifacts. J. Pathol. 221, 117–124 (2010). [PubMed: 20225337]
51. Sartori R et al. BMP signaling controls muscle mass. Nat. Genet. 45, 1309–1318 (2013). [PubMed: 24076600]
52. Winbanks CE et al. The bone morphogenetic protein axis is a positive regulator of skeletal muscle mass. J. Cell Biol. 203, 345–357 (2013). [PubMed: 24145169]
53. Tabebordbar M et al. Directed evolution of a family of AAV capsid variants enabling potent muscle-directed gene delivery across species. Cell 184, 4919–4938 (2021). [PubMed: 34506722]
54. Sonenberg N & Hinnebusch AG Regulation of translation initiation in eukaryotes: mechanisms and biological targets. Cell 136, 731–745 (2009). [PubMed: 19239892]
55. Madsen JGS et al. Integrated analysis of motif activity and gene expression changes of transcription factors. Genome Res. 28, 243–255 (2018). [PubMed: 29233921]
56. Amoasii L et al. NURR1 activation in skeletal muscle controls systemic energy homeostasis. Proc. Natl Acad. Sci. USA 116, 11299–11308 (2019). [PubMed: 31110021]
57. Tontonoz P et al. The orphan nuclear receptor Nur77 is a determinant of myofiber size and muscle mass in mice. Mol. Cell. Biol. 35, 1125–1138 (2015). [PubMed: 25605333]
58. Hendrickse P & Degens H The role of the microcirculation in muscle function and plasticity. J. Muscle Res. Cell Motil. 40, 127–140 (2019). [PubMed: 31165949]
59. Zhang W, Liu Y & Zhang H Extracellular matrix: an important regulator of cell functions and skeletal muscle development. Cell Biosci. 11, 65 (2021). [PubMed: 33789727]
60. Pereyra AS et al. Skeletal muscle undergoes fiber type metabolic switch without myosin heavy chain switch in response to defective fatty acid oxidation. Mol. Metab. 59, 101456 (2022). [PubMed: 35150906]
61. McKinsey TA, Zhang CL & Olson EN Control of muscle development by dueling HATs and HDACs. Curr. Opin. Genet Dev. 11, 497–504 (2001). [PubMed: 11532390]
62. Moresi V et al. Myogenin and class II HDACs control neurogenic muscle atrophy by inducing E3 ubiquitin ligases. Cell 143, 35–45 (2010). [PubMed: 20887891]
63. Dobin A et al. STAR: ultrafast universal RNA-seq aligner. Bioinformatics 29, 15–21 (2013). [PubMed: 23104886]
64. Heinz S et al. Simple combinations of lineage-determining transcription factors prime cis-regulatory elements required for macrophage and B cell identities. Mol. Cell 38, 576–589 (2010). [PubMed: 20513432]
65. Love MI, Huber W & Anders S Moderated estimation of fold change and dispersion for RNA-seq data with DESeq2. Genome Biol. 15, 550 (2014). [PubMed: 25516281]
66. Sun L et al. DiVenn: an interactive and integrated web-based visualization tool for comparing gene lists. Front. Genet. 10, 421 (2019). [PubMed: 31130993]
67. Tripathi S et al. Meta- and orthogonal integration of influenza 'OMICs' data defines a role for UBR4 in virus budding. Cell Host Microbe 18, 723–735 (2015). [PubMed: 26651948]
68. Metsalu T & Vilo J ClustVis: a web tool for visualizing clustering of multivariate data using principal component analysis and heatmap. Nucleic Acids Res. 43, W566–W570 (2015). [PubMed: 25969447]

69. Langmead B, Trapnell C, Pop M & Salzberg SL Ultrafast and memory-efficient alignment of short DNA sequences to the human genome. Genome Biol. 10, R25 (2009). [PubMed: 19261174]

70. McLen CY et al. GREAT improves functional interpretation of *cis*-regulatory regions. Nat. Biotechnol. 28, 495–501 (2010). [PubMed: 20436461]

71. Martin M Cutadapt removes adapter sequences from high-throughput sequencing reads. EMBnet J. 17, 10–12 (2011).

72. Zhong Y et al. RiboDiff: detecting changes of mRNA translation efficiency from ribosome footprints. Bioinformatics 33, 139–141 (2017). [PubMed: 27634950]

73. Liu Q, Shvarts T, Sliz P & Gregory RI RiboToolkit: an integrated platform for analysis and annotation of ribosome profiling data to decode mRNA translation at codon resolution. Nucleic Acids Res. 48, W218–W229 (2020). [PubMed: 32427338]

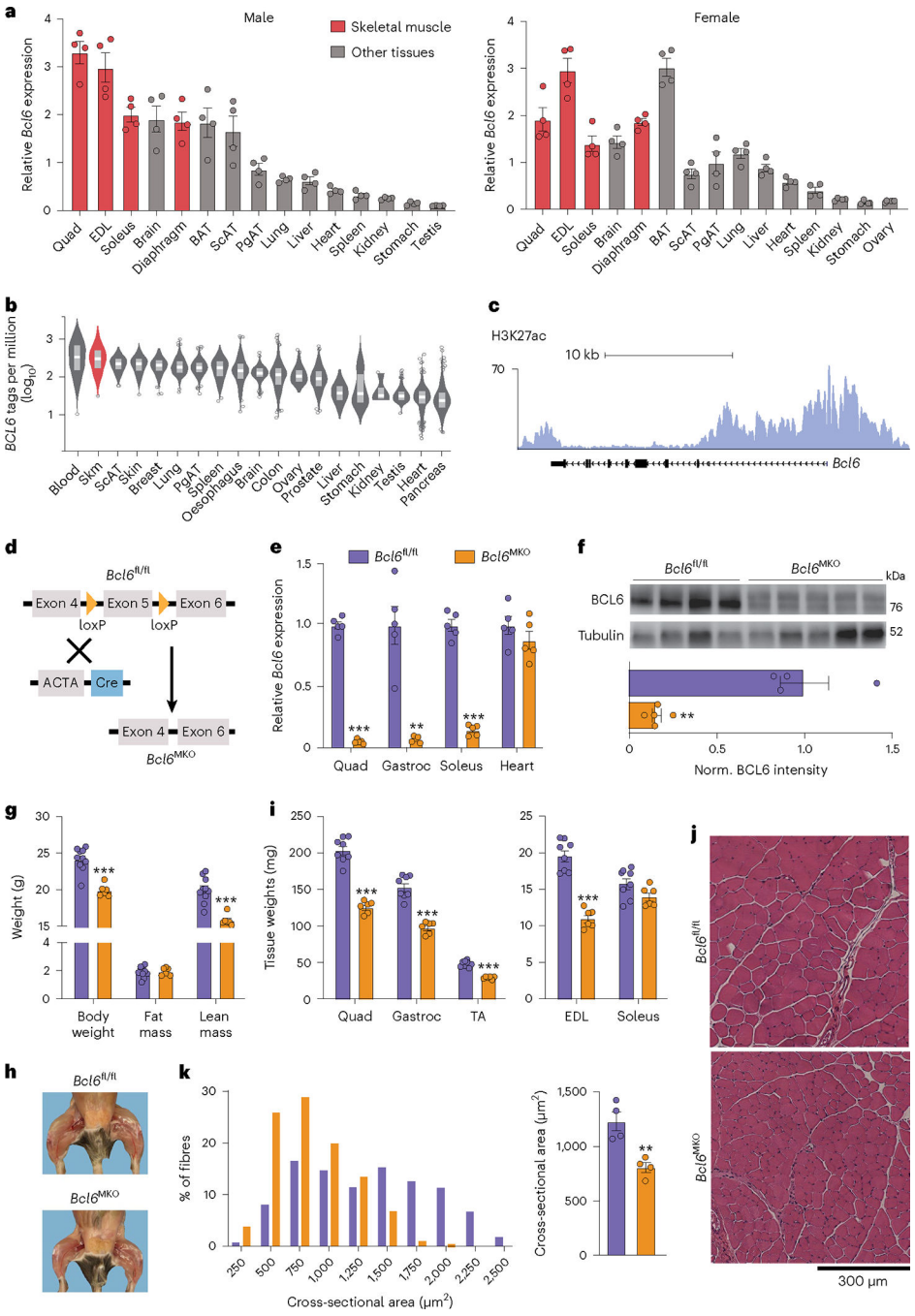

Fig. 1 |. *Bcl6* controls the development of skeletal muscle mass.

a, qPCR expression of *Bcl6* in C57BL/6 male and female mouse tissues relative to the housekeeping gene *36b4* (*n* = 4 per group). **b**, RNA-seq data for *BCL6* in 19 different human tissues from the GTEx database. The box plot shows the minimum to maximum tags per million values; the white bar indicates the median, and the grey rectangle represents the first to third quartile values. *N* is different for each tissue. **c**, ChIP–seq track for H3K27ac in quadriceps along the *Bcl6* gene revealed a super-enhancer. **d**, Schematic of mouse skeletal muscle-specific in utero *Bcl6* deletion model. Created with BioRender.com. **e**, qPCR

expression of *Bcl6* relative to the housekeeping gene *36b4* in quadriceps, gastrocnemius, soleus and heart from $Bcl6^{fl/fl}$ and $Bcl6^{MKO}$ mice ($n = 5$ per group). Unpaired, two-tailed *t*-test with Welch correction was performed. **f**, Western blot and densitometry of BCL6 and tubulin protein in quadriceps from $n = 4$ $Bcl6^{fl/fl}$ and $n = 5$ $Bcl6^{MKO}$ mice. $Bcl6^{fl/fl}$ versus $Bcl6^{MKO}$ $P = 0.0077$ by unpaired, two-tailed *t*-test with Welch correction. **g**, Total body weight, fat and lean mass in $n = 10$ $Bcl6^{fl/fl}$ and $n = 6$ $Bcl6^{MKO}$ male mice at 8 weeks of age. Unpaired, two-tailed *t*-test with Welch correction was performed. **h**, Representative image of lower limb muscles from $Bcl6^{fl/fl}$ and $Bcl6^{MKO}$ mice. **i**, Tissue weights of quadriceps, gastrocnemius, TA, EDL and soleus from $n = 8$ $Bcl6^{fl/fl}$ and $n = 6$ $Bcl6^{MKO}$ male mice at 16 weeks of age. Unpaired, two-tailed *t*-test with Welch correction was performed. **j**, H&E staining of representative TA muscle from 13-week-old male $Bcl6^{fl/fl}$ and $Bcl6^{MKO}$ mice. Scale bar, 300 μm. **k**, Myofibre CSAs determined from H&E-stained sections of TA from $Bcl6^{fl/fl}$ and $Bcl6^{MKO}$ mice ($n = 4$ per group). $Bcl6^{fl/fl}$ versus $Bcl6^{MKO}$ $P = 0.0095$ by unpaired, two-tailed *t*-test with Welch correction. All data are represented as the mean ± s.e.m. $^{**}P < 0.01$ and $^{***}P < 0.001$. BAT, brown adipose tissue; PgAT, perigonadal adipose tissue; Quad, quadriceps; ScAT, subcutaneous adipose tissue; Skm, skeletal muscle.

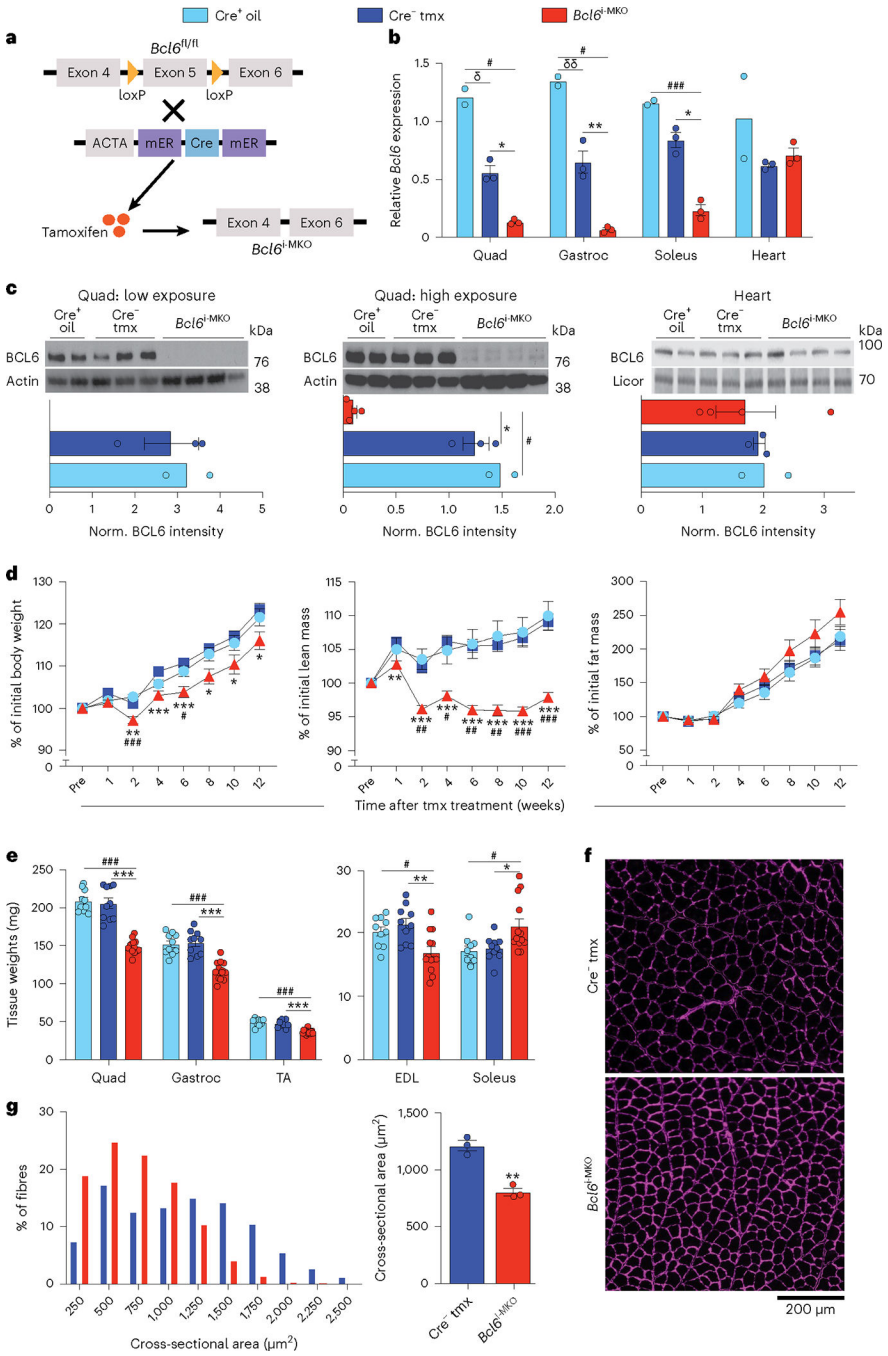

Fig. 2 |. Rapid muscle loss following muscle *Bcl6* deletion in adult mice.

a, Schematic of tamoxifen-inducible model for *Bcl6* deletion in adult mice. Created with BioRender.com. **b**, qPCR expression of *Bcl6* relative to the housekeeping gene *36b4* in quadriceps, gastrocnemius, soleus and heart from $n = 2$ Cre-positive oil-treated (Cre^+ oil), $n = 3$ Cre-negative tamoxifen-treated (Cre^- tmx) and $n = 3$ Cre-positive tamoxifen-treated ($Bcl6^{i\text{-}MKO}$) males 1 week after treatment. One-way analysis of variance (ANOVA) with Dunnett's multiple-comparisons test showed that in quadriceps, P(Cre^+ oil versus Cre^- tmx) = 0.0194, P(Cre^+ oil versus $Bcl6^{i\text{-}MKO}$) = 0.0011, P(Cre^- tmx versus $Bcl6^{i\text{-}MKO}$) = 0.0356;

in gastrocnemius, P(Cre$^+$ oil versus Cre$^-$ tmx) = 0.0090, P(Cre$^+$ oil versus *Bcl6*$^{i\text{-MKO}}$) = 0.0345, P(Cre$^-$ tmx versus *Bcl6*$^{i\text{-MKO}}$) = 0.0015; in soleus, P(Cre$^+$ oil versus *Bcl6*$^{i\text{-MKO}}$) = 0.0009, P(Cre$^-$ tmx versus *Bcl6*$^{i\text{-MKO}}$) = 0.0042. **c**, Western blot and densitometry of BCL6, actin, total (Licor) protein in quadriceps (left, short exposure; middle, long exposure) and heart (right) from n = 2 Cre$^+$ oil, n = 3 Cre$^-$ tmx and n = 4 *Bcl6*$^{i\text{-MKO}}$ males 1 week after tamoxifen or oil treatment. One-way ANOVA with Dunnett's multiple-comparisons test showed that P(Cre$^+$ oil versus *Bcl6*$^{i\text{-MKO}}$) = 0.0498 and P(Cre$^-$ tmx versus *Bcl6*$^{i\text{-MKO}}$) = 0.0240. **d**, Serial measurements of total body weight, lean and fat mass in n = 10 Cre$^+$ oil, n = 10 Cre$^-$ tmx and n = 13 *Bcl6*$^{i\text{-MKO}}$ male mice starting at 12 weeks of age before (pre) and up to 12 weeks after treatment. Two-way ANOVA with Tukey's multiple-comparisons test was performed. **e**, Tissue weights of quadriceps, gastrocnemius, TA, EDL and soleus from Cre$^+$ oil, Cre$^-$ tmx and *Bcl6*$^{i\text{-MKO}}$ male mice 12 weeks after treatment (n same as **d**). One-way ANOVA with Dunnett's multiple-comparisons test was performed. **f**, Laminin staining of representative TA muscle from Cre$^-$ tmx and *Bcl6*$^{i\text{-MKO}}$ male mice 6 weeks after tamoxifen treatment. Scale bar, 200 μm. **g**, Myofibre CSAs determined from laminin-stained sections (n = 3 per group; P = 0.0025 by unpaired, two-tailed t-test with Welch correction). All data are represented as the mean ± s.e.m. $^{\delta}P < 0.05$, $^{\delta\delta}P < 0.01$ for Cre$^+$ oil versus Cre$^-$ tmx; $^{\#}P < 0.05$, $^{\#\#}P < 0.01$, $^{\#\#\#}P < 0.001$ for Cre$^+$ oil versus *Bcl6*$^{i\text{-MKO}}$; $^{*}P < 0.05$, $^{**}P < 0.01$, $^{***}P < 0.001$ for Cre$^-$ tmx versus *Bcl6*$^{i\text{-MKO}}$.

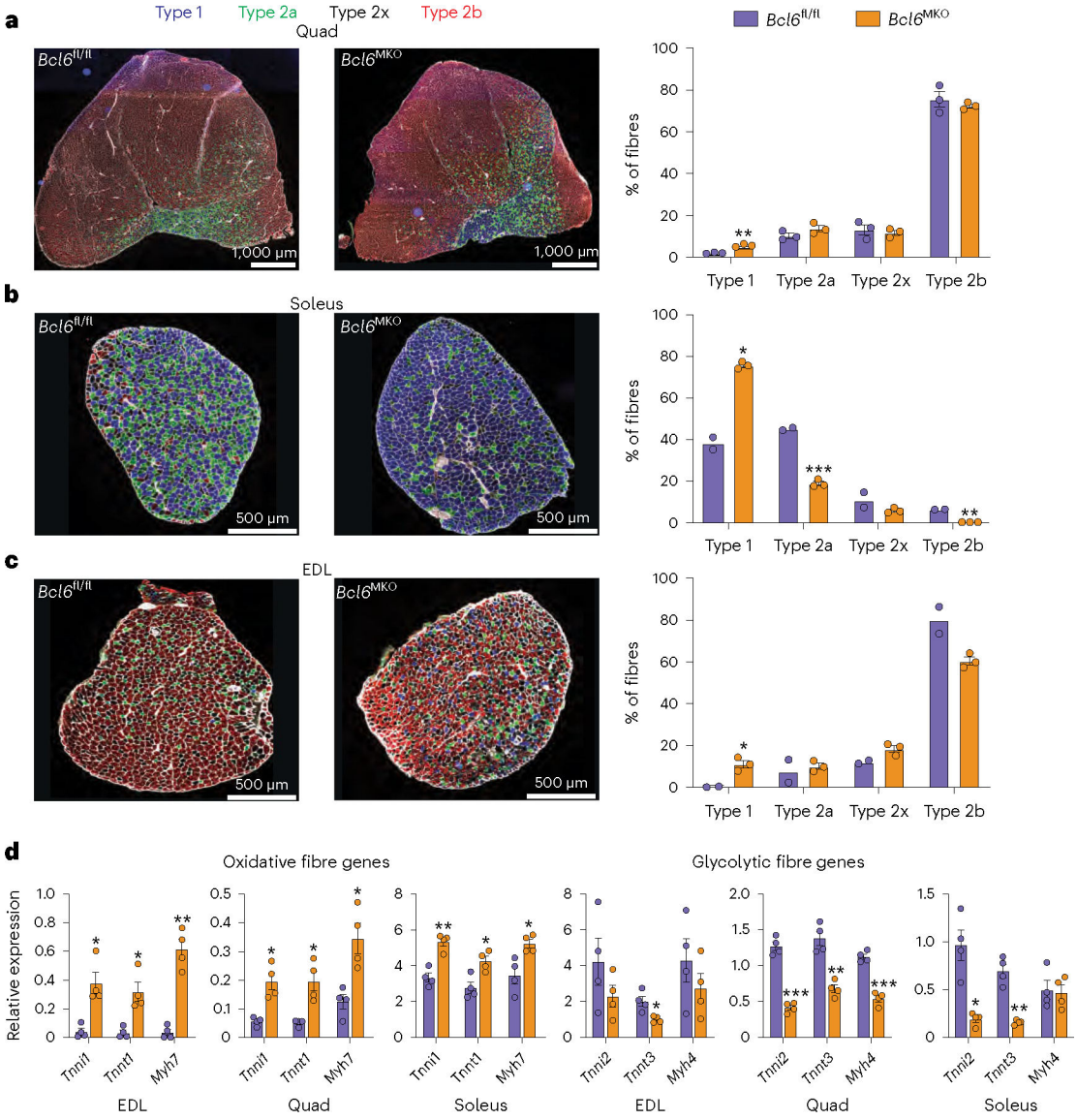

Fig. 3 |. *Bcl6* controls an oxidative to glycolytic shift in myofibres.

a–**c**, Representative fluorescent antibody-stained images of four myosin heavy chain isoforms in quadriceps (**a**), soleus (**b**) and EDL (**c**) from *Bcl6*$^{fl/fl}$ and *Bcl6*^{MKO} mice. MYH7 (type 1 fibre) is blue, MYH2 (type 2a fibre) is green, MYH1 (type 2x fibre) is black and MYH4 (type 2b fibre) is red. Quantification of fibre types is expressed as percentage of the total shown on the right (**a**, $n = 3$ per group; **b** and **c**, $n = 2$ *Bcl6*$^{fl/fl}$ and $n = 3$ *Bcl6*^{MKO} mice). *Bcl6*$^{fl/fl}$ versus *Bcl6*^{MKO} *P* value for type 1 fibre in quad = 0.0041, type 1 fibre in soleus = 0.0315, type 2a fibre in soleus = 0.0002, type 2b fibre in soleus = 0.0088 and type 1 fibre in EDL = 0.0266 by unpaired, two-tailed *t*-test with Welch correction. **d**, qPCR expression of oxidative and glycolytic genes relative to the housekeeping gene *36b4* in EDL, quadriceps and soleus from *Bcl6*$^{fl/fl}$ and *Bcl6*^{MKO} mice ($n = 4$ per group). *Bcl6*$^{fl/fl}$ versus *Bcl6*^{MKO}; EDL: *P* value for *Tnni1* = 0.0175, *Tnnt1* = 0.02, *Myh7* = 0.0019, *Tnnt3* = 0.0334; *Bcl6*$^{fl/fl}$ versus *Bcl6*^{MKO}; quadriceps: *P* value for *Tnni1* = 0.0147, *Tnnt1* = 0.0238, *Myh7* = 0.0174, *Tnni2* = 0.0001, *Tnnt3* = 0.0021, *Myh4* = 0.00008; *Bcl6*$^{fl/fl}$ versus *Bcl6*^{MKO}; soleus:

P value for *Tnni1* = 0.0012, *Tnnt1* = 0.0125, *Myh7* = 0.0267, *Tnni2* = 0.0242, *Tnnt3* = 0.0042 by unpaired, two-tailed *t*-test with Welch correction. All data are represented as the mean ± s.e.m. **P* < 0.05, ***P* < 0.01 and ****P* < 0.001.

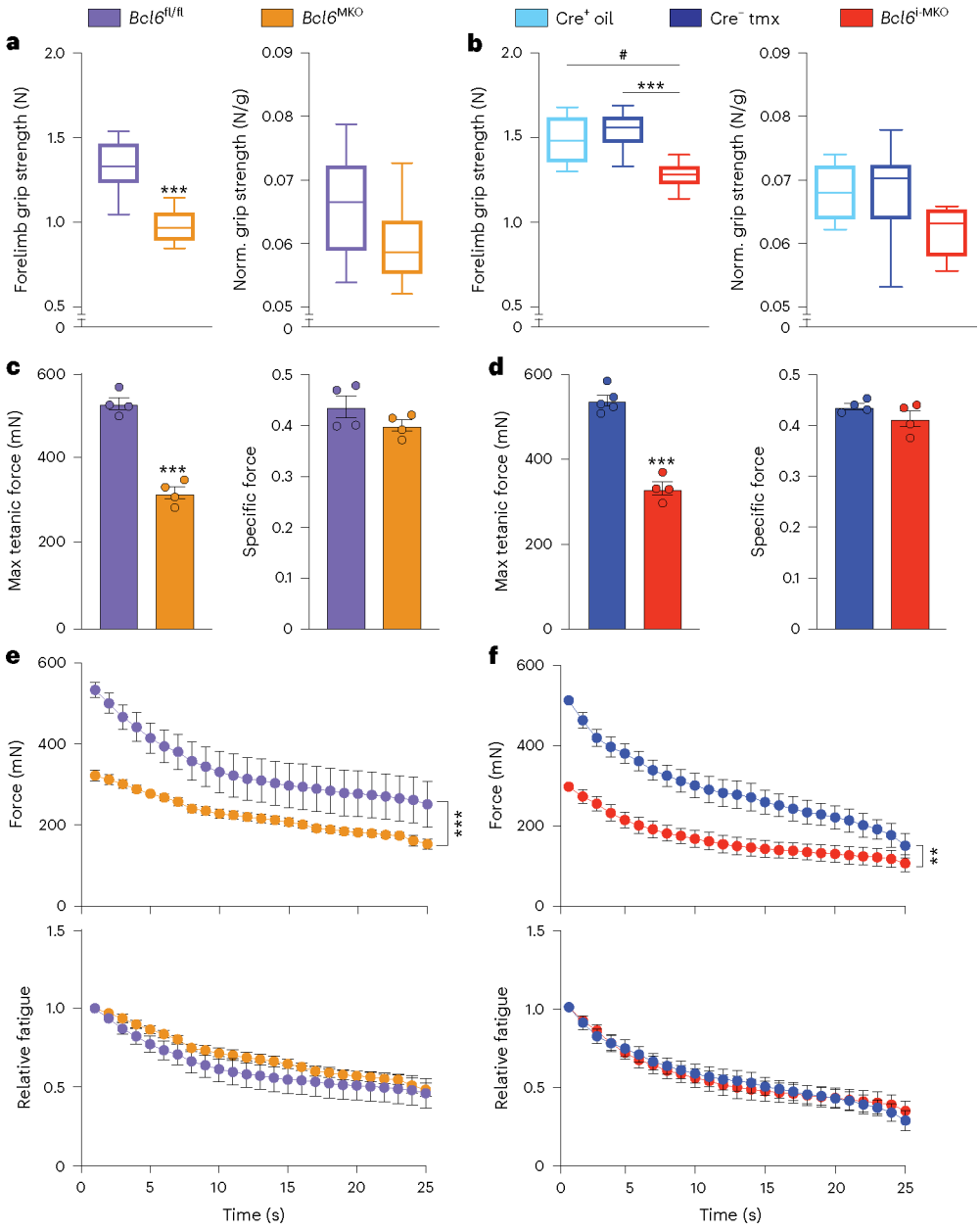

Fig. 4 |. *Bcl6* enhances skeletal muscle force production.

a,**b**, Absolute (left) and lean body mass normalized (right) forelimb grip strength measured in $n = 10$ $Bcl6^{fl/fl}$ and $n = 6$ $Bcl6^{MKO}$ male mice at 12 weeks of age (P value for absolute grip strength = 0.00007 by unpaired, two-tailed t-test with Welch correction) (**a**) and $n =$ 6 Cre^{+} oil, $n = 9$ Cre^{-} tmx and $n = 9$ $Bcl6^{i\text{-}MKO}$ male mice 12 weeks after tamoxifen or oil treatment (**b**). One-way ANOVA with Dunnett's multiple-comparisons test for absolute grip strength showed that $P(Cre^{+}$ oil versus $Bcl6^{iMKO}) = 0.0390$ and $P(Cre^{-}$ tmx versus $Bcl6^{i\text{-}MKO}) = 0.0001$. Whiskers in the box plot show the minimum to maximum values, the line indicates the median and the box represents the first to third quartile values. **c**,**d**, Maximum tetanic force (left) and specific force (right) for TA muscle from 13-week-old $Bcl6^{fl/fl}$ and $Bcl6^{MKO}$ male mice ($n = 4$ per group; P value for max force = 0.00004

by unpaired, two-tailed *t*-test with Welch correction) (**c**) and $n = 5$ Cre^- tmx and $n = 4$ $Bcl6^{i\text{-}MKO}$ male mice 6 weeks after tamoxifen treatment (P value for maximum force = 0.00003 by unpaired, two-tailed *t*-test with Welch correction) (**d**). **e**,**f**, Fatigue curves showing the decline in force production by the TA muscle from 13-week-old $Bcl6^{fl/fl}$ and $Bcl6^{MKO}$ male mice ($n = 4$ per group; P value for fatigue $< 1 \times 10^{-15}$ by two-way ANOVA) (**e**) and $n = 5$ Cre^- tmx and $n = 4$ $Bcl6^{i\text{-}MKO}$ male mice 6 weeks after tamoxifen treatment (P value for fatigue = 0.0088 by two-way ANOVA) (**f**) over 25 consecutive bouts of isometric contraction. Relative fatigue calculated by dividing each value by the initial force is shown at the bottom. All data are represented as the mean ± s.e.m. $^{\#}P < 0.05$ for Cre^+ oil versus $Bcl6^{i\text{-}MKO}$ and $^{**}P < 0.01$, $^{***}P < 0.001$ for Cre^- tmx versus $Bcl6^{i\text{-}MKO}$.

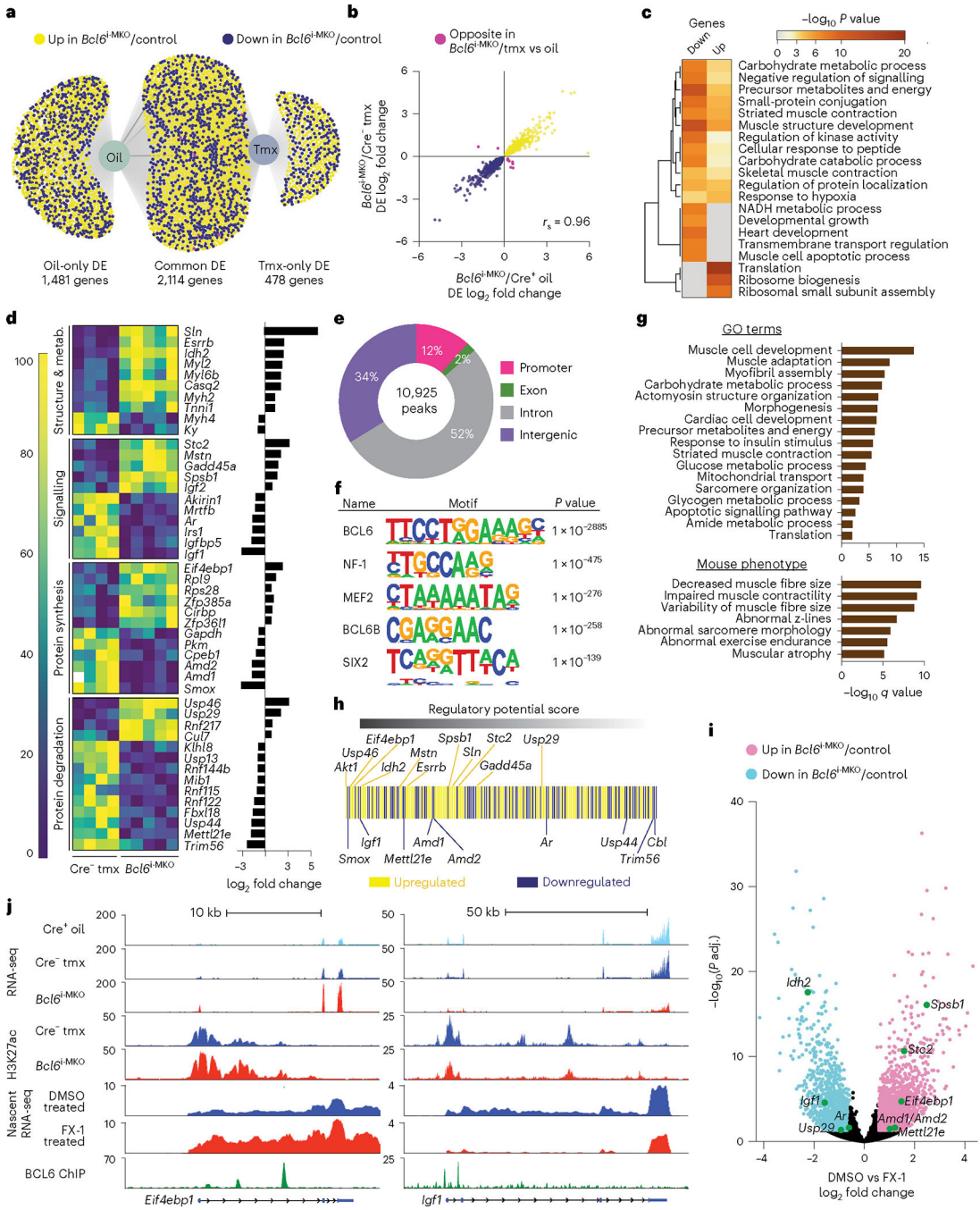

Fig. 5 |. BCL6 directly controls the expression of anabolic regulators.

a, Venn diagram depicting DE muscle genes between $n = 5$ *Bcl6*$^{i\text{-MKO}}$ and $n = 4$ tamoxifen-treated controls (Cre^{-} tmx) or $n = 4$ corn oil-treated controls (Cre^{+} oil). DE genes identified in both are in the centre. DE genes specific to *Bcl6*$^{i\text{-MKO}}$ and Cre^{-} tmx (right) or *Bcl6*$^{i\text{-MKO}}$ and Cre^{+} oil (left) are also shown. **b**, Quadrant plot of $\log_2$ fold change in gene expression for common DE genes in *Bcl6*$^{i\text{-MKO}}$/Cre^{-} tmx versus $\log_2$ fold change in *Bcl6*$^{i\text{-MKO}}$/Cre^{+} oil. Spearman correlation coefficient $r_S = 0.96$. **c**, Ontology analysis of DE downregulated (left column) and upregulated (right column) genes in *Bcl6*$^{i\text{-MKO}}$ mice

compared to both controls. Cumulative hypergeometric statistical test was used. **d**, Heat map of FPKM values for selected genes in muscle samples from *Bcl6*$^{i\text{-MKO}}$ and Cre^{-} tmx mice. Colours represent expression from maximum (yellow) to minimum (blue) for each gene. Log_2 fold change in expression for *Bcl6*$^{i\text{-MKO}}$ samples versus Cre^{+} oil controls are also shown (right). **e**, Pie chart showing genomic distribution of BCL6 binding sites in C57BL/6 mouse quadriceps. **f**, Top motifs enriched near BCL6 peaks and *P* values calculated with cumulative hypergeometric statistical testing. **g**, Top biological process (top) and mouse phenotype (bottom) ontologies for genes near BCL6 peaks. Cumulative hypergeometric statistical testing was used. **h**, Integrated RNA-seq and ChIP–seq analysis using Cistrome-GO depicting the likelihood that a gene is regulated by BCL6 (rank product score). Genes with log_2 fold change expression > 1 in *Bcl6*$^{i\text{-MKO}}$/Cre^{-} tmx and annotated BCL6 binding sites are shown. **i**, Volcano plot showing upregulated (pink) and downregulated (light blue) BCL6 target genes from nascent RNA-seq in C57BL/6 mice exposed to the BCL6 inhibitor FX-1 (50 mg per kg body weight) compared to vehicle-treated controls for 3 h ($n = 5$ per group). Wald test was used to calculate the *P* values. **j**, UCSC browser tracks of RNA-seq in quadriceps from Cre^{+} oil, Cre^{-} tmx and *Bcl6*$^{i\text{-MKO}}$ mice, H3K27ac ChIP–seq in quadriceps from Cre^{-} tmx and *Bcl6*$^{i\text{-MKO}}$ mice 1 week after oil or tamoxifen treatment, nascent RNA-seq in quadriceps from mice treated with DMSO or FX-1 for 3 h, and BCL6 ChIP–seq track in quadriceps from C57BL/6 animals along the *Eif4ebp1* (left) and *Igf1* (right) genes.

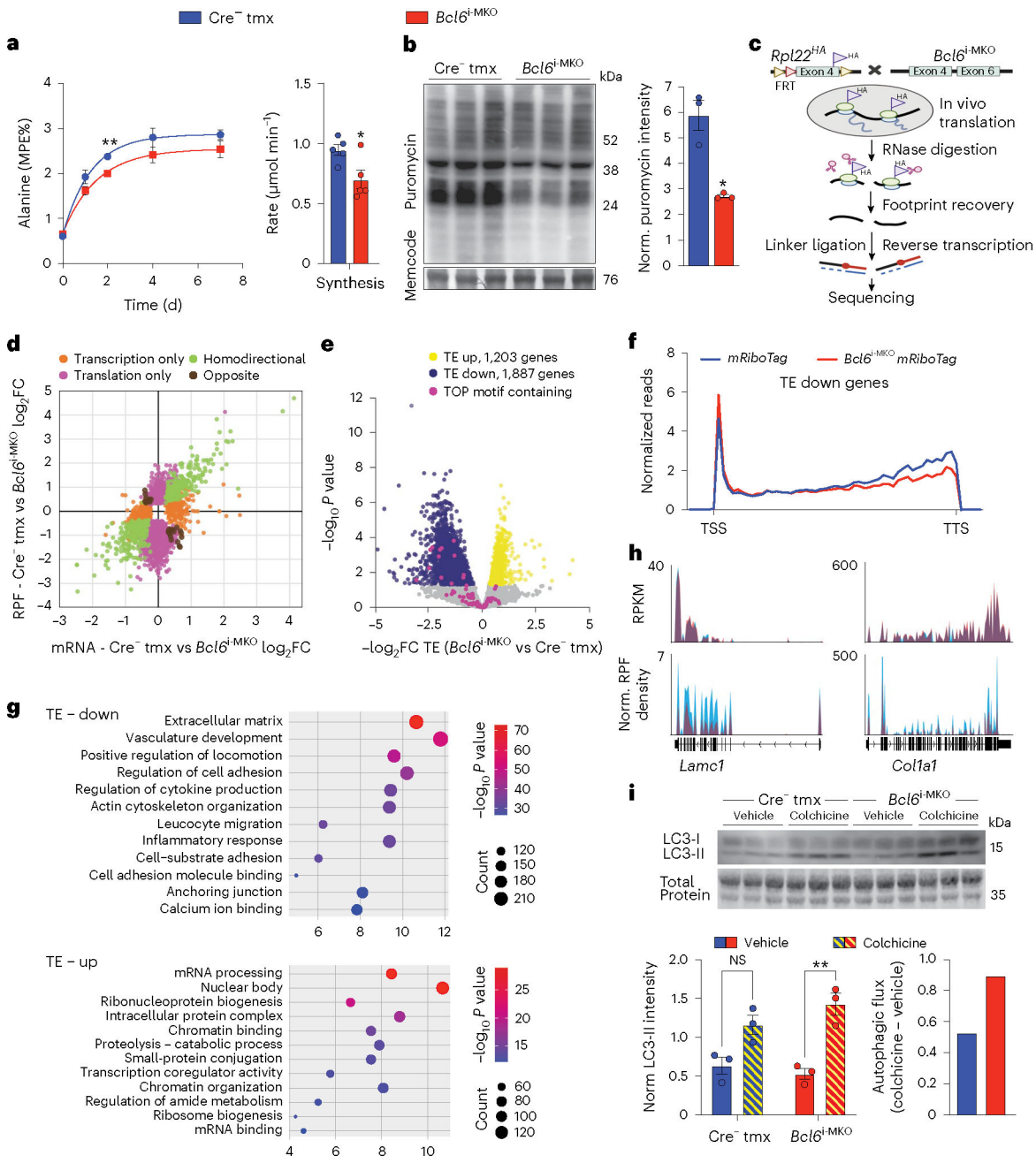

Fig. 6 |. Loss of *Bcl6* reduces the rate of muscle protein synthesis.

a, Temporal profile for alanine labelling (MPE, moles percent excess) in quadriceps of Cre^{-} tmx and *Bcl6*$^{i\text{-MKO}}$ mice following ^{2}H-saline injection 1 week after tamoxifen treatment ($n = 4$ Cre^{-} tmx mice for days 0, 1 and 2 and $n = 5$ Cre^{-} tmx mice for days 4 and 7; $n = 4$ *Bcl6*$^{i\text{-MKO}}$ for day 0 and $n = 5$ *Bcl6*$^{i\text{-MKO}}$ for days 1, 2, 4 and 7); P value on day 2 = 0.0064 by unpaired, two-tailed t-test with Welch correction. Calculated rates of muscle protein synthesis on the right ($n = 5$ per group). $P = 0.0319$ by unpaired, two-tailed t-test with Welch correction. **b**, SUnSET analysis of puromycin incorporation into quadriceps in Cre^{-} tmx and *Bcl6*$^{i\text{-MKO}}$ mice 1.5 weeks after tamoxifen treatment.

Puromycin labelling relative to total protein (Memcode) by densitometry (right; $n = 3$ per group; $P = 0.0315$ by unpaired, two-tailed t-test with Welch correction). **c**, Schematic of *Bcl6*$^{i\text{-MKO}}$*mRiboTag* mouse model and Ribo-seq procedure. Created with BioRender.com. **d**, Quadrant plot showing $\log_2$ fold change of RPFs versus $\log_2$ fold change of mRNA for *Bcl6*$^{i\text{-MKO}}$*mRiboTag*/*mRiboTag* quadriceps 3 weeks after tamoxifen treatment. **e**, Volcano plot of TE. Significantly upregulated TE genes (yellow), downregulated TE genes (blue), known mRNAs with 5′ TOP motifs (pink) and non-significantly altered genes (grey) are plotted ($n = 4$ per group). Wald test was used to calculate the P values. **f**, Metagene distribution plot showing normalized Ribo-seq RPF reads from the TSS to transcription termination site (TTS) for genes with reduced TE. **g**, GO for transcripts with significantly altered TE. Cumulative hypergeometric statistical test was used. **h**, Browser tracks showing mRNA RPKM (top) and normalized RPF density (bottom) in quadriceps from *mRiboTag* and *Bcl6*$^{i\text{-MKO}}$*mRiboTag* mice along *Lamc1* and *Col1a1* genes. **i**, Western blot and densitometry of LC3 and total protein (Licor) in quadriceps from Cre^{-} tmx and *Bcl6*$^{i\text{-MKO}}$ males 1.5 weeks after tamoxifen and following colchicine or vehicle treatment ($n = 3$ per group). Two-way ANOVA followed by Tukey's multiple-comparisons test was performed. Flux is the difference in average LC3-II levels in colchicine minus vehicle (bottom right). Data in **a**, **b** and **i** are represented as the mean ± s.e.m. *$P < 0.05$ and **$P < 0.01$. NS, not significant.

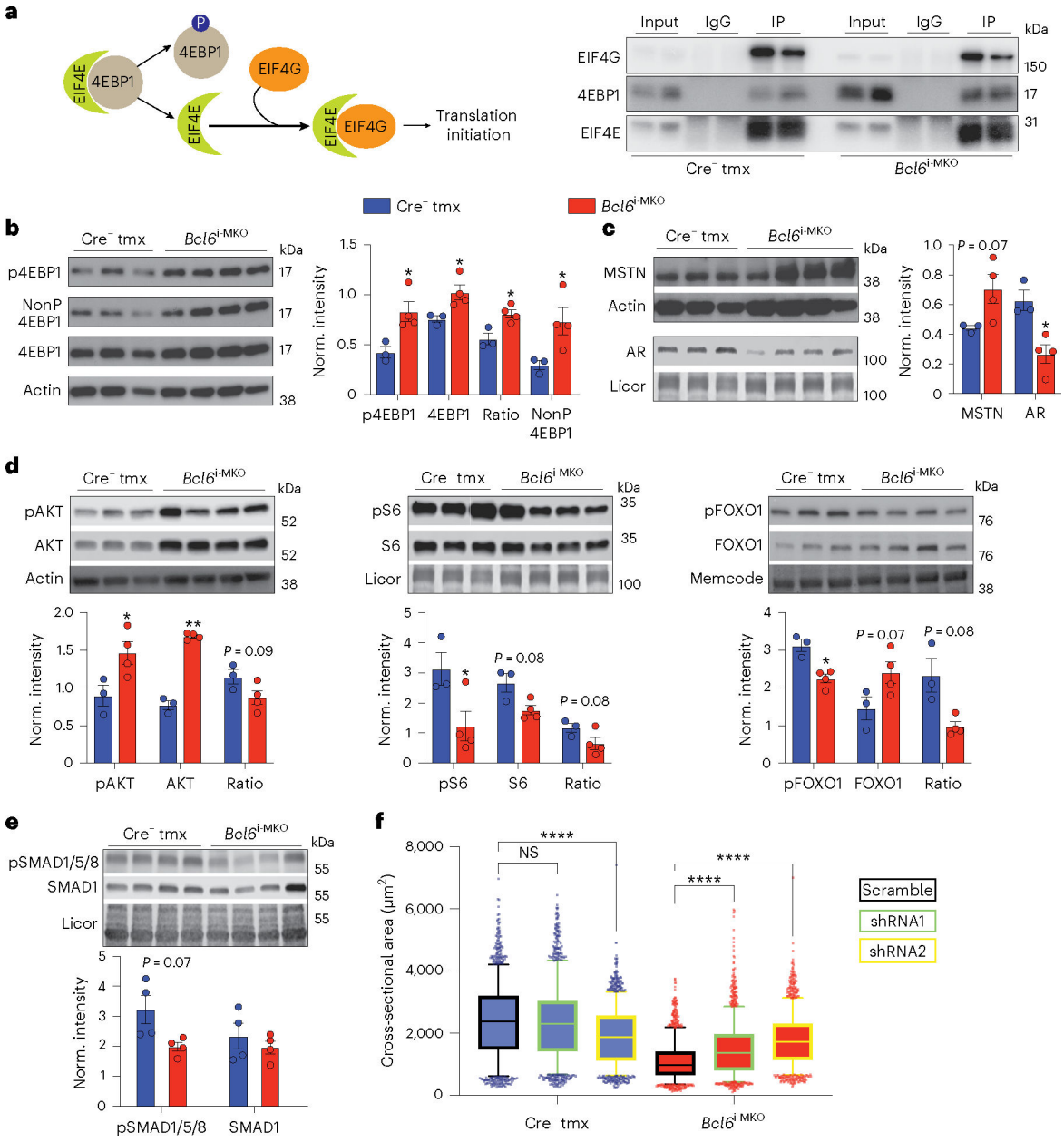

Fig. 7 |. BCL6 controls translation in skeletal muscle.

a, Left: schematic of EIF4E's interaction with 4EBP1 and EIF4G. Right: EIF4E co-immunoprecipitation and western blots for EIF4G (top), 4EBP1 (middle) and EIF4E (bottom) in quadriceps from Cre⁻ tmx and *Bcl6*$^{i\text{-}MKO}$ males 1 week after tamoxifen treatment ($n = 2$ per group). **b**, Western blot and densitometry of p4EBP1, non-phospho-4EBP1, total 4EBP1 and actin protein in gastrocnemius from $n = 3$ Cre⁻ tmx and $n = 4$ *Bcl6*$^{i\text{-}MKO}$ males 1 week after treatment. Cre⁻ tmx versus *Bcl6*$^{i\text{-}MKO}$ *P* value for p4EBP1 = 0.0188, total 4EBP1 = 0.0319, ratio = 0.0258 and non-phospho-4EBP1 = 0.0426 by unpaired, two-tailed *t*-test with Welch correction. **c**,**d**, Western blot and densitometry of myostatin, AR (**c**), IGF-1–AKT signalling (**d**; pAKT, AKT, pS6, S6, pFOXO1, FOXO1) and actin or total (Licor, Memcode) protein in quadriceps from $n = 3$ Cre⁻ tmx and $n =$

4 *Bcl6*$^{i\text{-MKO}}$ males 1 week after treatment. Cre^{-} tmx versus *Bcl6*$^{i\text{-MKO}}$ *P* value for AR = 0.0133, pAKT = 0.0383, total AKT = 0.0016, pS6 = 0.048 and pFOXO1 = 0.0126 by unpaired, two-tailed *t*-test with Welch correction. **e**, Western blot and densitometry of pSMAD1/pSMAD5/pSMAD8, total SMAD1 and total (Licor) protein in quadriceps from Cre^{-} tmx and *Bcl6*$^{i\text{-MKO}}$ males 1 week after treatment ($n = 4$ per group). **f**, Myofibre CSAs determined from skeletal muscle of Cre^{-} tmx and *Bcl6*$^{i\text{-MKO}}$ mice infected with MyoAAV4As encoding scramble (Scrmb) or *Eif4ebp1* shRNAs and then treated with tamoxifen. CSAs of 2,000 myofibres per mouse were determined 8 weeks later ($n = 3$ mice per group for scramble and *Eif4ebp1* shRNA1 and $n = 2$ mice per group for *Eif4ebp1* shRNA2). Whiskers in the box plot show 5–95th percentile values, the line indicates the median, and the box represents the first to third quartile values. Two-way ANOVA followed by Tukey's multiple-comparisons test was performed. *P* value $< 1 \times 10^{-15}$ for Scrmb-Cre^{-} tmx versus shRNA2-Cre^{-} tmx, Scrmb-Cre^{-} tmx versus Scrmb-*Bcl6*$^{i\text{-MKO}}$, Scrmb-Cre^{-} tmx versus shRNA1-*Bcl6*$^{i\text{-MKO}}$, Scrmb-Cre^{-} tmx versus shRNA2-*Bcl6*$^{i\text{-MKO}}$, shRNA1-Cre^{-} tmx versus shRNA2-Cre^{-} tmx, shRNA1-Cre^{-} tmx versus Scrmb-*Bcl6*$^{i\text{-MKO}}$, shRNA1-Cre^{-} tmx versus shRNA1-*Bcl6*$^{i\text{-MKO}}$, shRNA1-Cre^{-} tmx versus shRNA2-*Bcl6*$^{i\text{-MKO}}$, shRNA2-Cre^{-} tmx versus Scrmb-*Bcl6*$^{i\text{-MKO}}$, shRNA2-Cre^{-} tmx versus shRNA1-*Bcl6*$^{i\text{-MKO}}$, shRNA2-Cre^{-} tmx versus shRNA2-*Bcl6*$^{i\text{-MKO}}$, Scrmb-*Bcl6*$^{i\text{-MKO}}$ versus shRNA1-*Bcl6*$^{i\text{-MKO}}$, Scrmb-*Bcl6*$^{i\text{-MKO}}$ versus shRNA2-*Bcl6*$^{i\text{-MKO}}$ and shRNA1-*Bcl6*$^{i\text{-MKO}}$ versus shRNA2-*Bcl6*$^{i\text{-MKO}}$. All data are represented as the mean ± s.e.m. $*P < 0.05$, $**P < 0.01$ and $****P < 0.0001$.

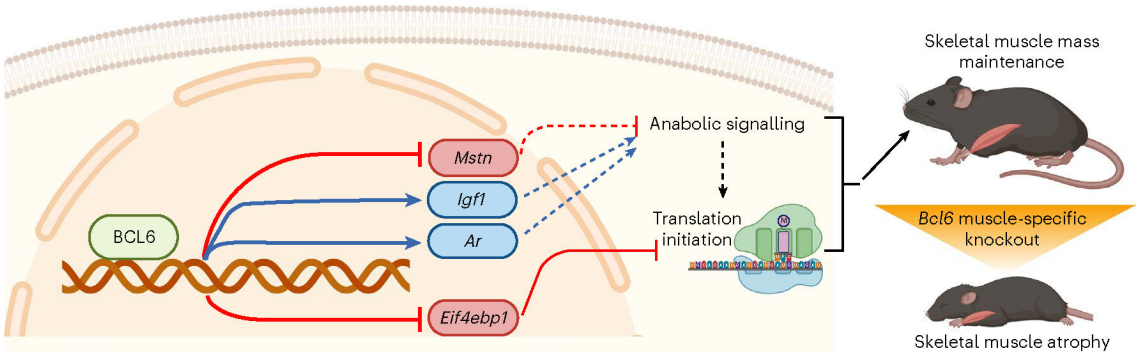

Fig. 8 |. Model for BCL6-mediated control of skeletal muscle proteostasis.

BCL6-mediated transcriptional regulation controls the expression of atrogenic regulators to establish and maintain skeletal muscle mass. BCL6 directly represses *Eif4ebp1* and possibly *Mstn*, while it directly activates *Igf1* and *Ar*. Loss of *Bcl6* in muscle acutely reduces cap-dependent translation and anabolic signalling, resulting in reduced protein synthesis, increased autophagy and skeletal muscle atrophy. Created with BioRender.com.